A&A 551, A34 (2013)
DOI: 10.1051/0004-6361/201220170

Astronomy & Astrophysics

Protostars, multiplicity, and disk evolution in the Corona Australis region: a *Herschel* Gould Belt Study⋆,⋆⋆

A. Sicilia-Aguilar[1], T. Henning[2], H. Linz[2], P. André[3], A. Stutz[2], C. Eiroa[1], and G. J. White[4,5]

[1] Departamento de Física Teórica, Facultad de Ciencias, Universidad Autónoma de Madrid, 28049 Cantoblanco, Madrid, Spain
e-mail: aurora.sicilia@uam.es
[2] Max-Planck-Institut für Astronomie, Königstuhl 17, 69117 Heidelberg, Germany
[3] Laboratoire AIM, CEA/DSM–CNRS–Université Paris Diderot, IRFU/Service d'Astrophysique, CEA Saclay, 91191 Gif-sur-Yvette, France
[4] RAL Space, STFC Rutherford Appleton Laboratory, Chilton, Didcot, Oxfordshire, OX11 0QX, UK
[5] Department of Physical Sciences, The Open University, Walton Hall, Milton Keynes, MK7 6AA, UK

Received 6 August 2012 / Accepted 27 November 2012

ABSTRACT

Context. The CrA region and the Coronet cluster form a nearby (138 pc), young (1−2 Myr) star-forming region that hosts a moderate population of Class I, II, and III objects.
Aims. We study the structure of the cluster and the properties of the protostars and protoplanetary disks in the region.
Methods. We present *Herschel* PACS photometry at 100 and 160 μm, obtained as part of the *Herschel* Gould Belt Survey. The *Herschel* maps reveal the cluster members within the cloud with high sensitivity and high dynamic range.
Results. Many of the cluster members are detected, including some embedded, very low-mass objects, several protostars (some of them extended), and substantial emission from the surrounding molecular cloud. *Herschel* also reveals some striking structures, such as bright filaments around the IRS 5 protostar complex and a bubble-shaped rim associated with the Class I object IRS 2. The disks around the Class II objects display a wide range of mid- and far-IR excesses consistent with different disk structures. We have modeled the disks with the RADMC radiative transfer code to quantify their properties. Some of them are consistent with flared, massive, relatively primordial disks (S CrA, T CrA). Others display significant evidence for inside-out evolution, consistent with the presence of inner holes/gaps (G-85, G-87). Finally, we found disks with a dramatic small dust depletion (G-1, HBC 677) that, in some cases, could be related to truncation or to the presence of large gaps in a flared disk (CrA-159). The derived masses for the disks around the low-mass stars are found to be below the typical values in Taurus, in agreement with previous *Spitzer* observations.
Conclusions. The Coronet cluster presents itself as an interesting compact region that contains both young protostars and very evolved disks. The *Herschel* data provide sufficient spatial resolution to detect small-scale details, such as filamentary structures or spiral arms associated with multiple star formation. The disks around the cluster members range from massive, flared primordial disks to disks with substantial small dust grain depletion or with evidence of inside-out evolution. This results in an interesting mixture of objects for a young and presumably coevally formed cluster. Given the high degree of multiplicity and interactions observed among the protostars in the region, the diversity of disks may be a consequence of the early star formation history, which should also be taken into account when studying the disk properties in similar sparsely populated clusters.

Key words. stars: formation – stars: pre-main sequence – protoplanetary disks – stars: late-type

1. Introduction

The Corona Australis (CrA) star-forming region is a nearby, large (~13 pc; Graham 1992) molecular cloud, located out of the Galactic plane. It is populated by a few young, intermediate-mass stars and a sparse cluster, known as the Coronet cluster. Marraco & Rydgren (1981) identified a compact group of pre-main-sequence stars, and Ortiz et al. (2010) confirmed a distance of 138 ± 16 pc based on light echoes, which places the cluster among the closest, brightest and most compact star-forming regions. The Coronet cluster is an obscured, compact (<1.1 pc across) region associated with the Ae star R CrA (Taylor & Storey 1984) and a dense molecular core (Loren 1979; Harju et al. 1993). The presence of several far-IR sources revealed some embedded young stars (de Muizon et al. 1980; Wilking et al. 1985; Henning et al. 1994). X-ray observations with Einstein, *XMM-Newton*, ROSAT, and *Chandra* (Walter 1986, 1997; Neuhäuser et al. 1997, 2000; Garmire & Garmire 2003; Hamaguchi et al. 2005; Forbrich & Preibisch 2007), which are less affected by dust extinction, extended the initial identification of intermediate-mass stars to a large number of low-mass members. This revealed a quite rich cluster with several Class I protostars, some of which show strong X-ray flares. Combined X-ray and radio observations (Forbrich et al. 2006) confirmed these results. Deep X-ray observations revealed a large number (>70, Garmire & Garmire 2003) of sources that could be associated with young stars, many of which are deeply embedded. Independently, IR observations (including *Spitzer*) revealed more than 100 sources (Class I, Class II, and Class III objects), some of them highly extincted, suggesting ages clearly younger than 2−3 Myr (Nisini et al. 2005; Peterson et al. 2011; Sicilia-Aguilar et al. 2011a). These very

⋆ *Herschel* is an ESA space observatory with science instruments provided by European-led Principal Investigator consortia and with important participation from NASA.
⋆⋆ Table 3 is available in electronic form at http://www.aanda.org

young ages agree with the detection of ongoing star formation and Class 0 candidates (Wang et al. 2004; Nutter et al. 2005; Chen & Arce 2010). Finally, optical spectroscopy of some of the X-ray and *Spitzer* sources revealed a rich variety of accreting and non-accreting T Tauri stars (TTS) and brown dwarf (BD) candidates with spectral types K7-M8 and different disk morphologies (Sicilia-Aguilar et al. 2008, 2011a). The disk fraction was suggested to be about 65% (Sicilia-Aguilar et al. 2008), although the discovery of new diskless members lowered it to ∼50% for the M-type objects (López-Martí et al. 2010). Isochrone fitting to the extinction-corrected JHK photometry revealed an age younger than 2 Myr for the low-mass TTS in the region (Sicilia-Aguilar et al. 2011a).

Given that the Coronet cluster is one of the most interesting regions for studies of low-mass star formation, several millimeter and submillimeter studies have concentrated on identifying the earlier phases of the process (Henning et al. 1994; Chini et al. 2003; Groppi et al. 2004, 2007; Nutter et al. 2005). The 1.3 mm study of Henning et al. (1994) had a mass sensitivity limit of around 5×10^{-4} $M_{\odot}$ in cold dust, revealing the presence of disks and structures around the Herbig Ae/Be stars and massive TTS. The study of Chini et al. (2003) reached a higher sensitivity at 1.3 mm and identifyed 25 individual emission sources within a $15' \times 30'$ area containing the cluster center and its southern part around VV CrA. By comparison with other observations, these objects could be traced back to disks around K- and earlier-type stars, embedded protostellar sources, and more diffuse ambient cloud emission. Groppi et al. (2004) mapped the densest part of the cloud in its 870 μm continuum emission, but the survey avoided the less dense regions that contain most of the Class II/III objects. Nutter et al. (2005) and Groppi et al. (2007) used SCUBA to obtain a higher resolution map of the region, which covered the central part around the emission peak in IRS 7. They resolved several peaks in this region, including a potential Class 0 protostar. APEX/LABOCA mapping of the region at 870 μm confirmed the presence of dense structures associated with embedded objects, but also revealed starless regions with lower column densities, suggestive of inefficient star formation, although the low spatial resolution did not allow one to study the details in the cluster center (Sicilia-Aguilar et al. 2011a).

Here we present observations of the CrA region obtained with the ESA *Herschel* Space Observatory (Pilbratt et al. 2010) using the PACS bolometer (Poglitsch et al. 2010) at 100 and 160 μm. The observations are part of the *Herschel* Gould Belt Survey (cf. André et al. 2010 and http://gouldbelt-herschel.cea.fr). The *Herschel*/PACS data reveal the structure of the CrA star-forming region and the properties of its protostellar and disk population with unprecedent mapping speed, sensitivity, dynamic range, and spatial resolution. In Sect. 2 we describe the *Herschel* observations and data reduction, as well as other complementary data. In Sect. 3 we study the properties of the individual objects, and Sect. 4 presents the implications for intermediate-mass and low-mass star formation. We also derive disk parameters by fitting the SEDs of the objects with the radiative transfer code RADMC. Finally, we summarize our results in Sect. 5.

2. Observations and data reduction

2.1. Herschel/PACS observations

Broad-band continuum data were taken with the Photodetector Array Camera & Spectrometer (PACS, Pilbratt et al. 2010) on board the *Herschel* spacecraft. The data were obtained as part of the *Herschel* Gould Belt Survey (André et al. 2010, see http://gouldbelt-herschel.cea.fr/archives) in a similar way as the rest of Gould Belt targets. Square scan maps with an extent of almost 89 arcmin on a side were obtained simultaneously in the 100 and 160 μm filters on April 18, 2011. The nominal scan speed was 20″/s. For the first stage of the data reduction we used customized Jython scripts within the HIPE[1] environment, version 7.3.0 (Ott et al. 2010). In addition to the standard steps intended to calibrate the raw data from internal units to Jy/pixel and to remove glitches and other bad data in the scan time lines, we applied corrections for electronic cross talk as well as for non-linearity in the PACS detector response for the brightest compact sources. These so-called level-1 data were further processed with SCANAMORPHOS (Roussel 2012). This program has its own heuristic algorithms to remove artifacts caused by detector flickering noise as well as spurious bolometer temperature drifts, which is better suited for the extended emission compared to the standard approach of high-pass filtering that is implemented in HIPE. We used version 14 of SCANAMORPHOS. The field of view of the entire maps is large and contains large areas with low emission (especially in the 100 μm map). Since we are mainly interested in the CrA point sources, we did not apply the GALACTIC option that is used if high background levels and extended emission dominate the maps. The final maps were projected onto a 2″/pixel grid (100 μm) and 3″ pixel (160 μm) within SCANAMORPHOS and were written out as fits files for further analysis.

The photometry was performed on the final map (see Tables 1 and 2). Given the characteristics of our objects (usually either relatively faint targets or extended sources), we chose to perform aperture photometry. For non-extended (or marginally extended) point-like sources, we used IRAF[2] tasks *daofind* and *apphot* to extract the positions of the sources and to perform aperture photometry. We applied the apertures and sky parameters used for the DUNES program (Mora, private communication) to maximize the signal-to-noise ratio (S/N), namely apertures of 5″ for the 100 μm band, and 8″ for the 160 μm band, with their corresponding aperture corrections of 1.949 (100 μm) and 1.919 (160 μm). The sky regions were selected according to the local background of each individual source, given the enormous variability of the cloud and background emission in few-arcsec scales. In general, large separations between the source and the sky annulus would ensure that the fraction of source flux within the sky annulus is minimal, but for objects with nearby sources or variable cloud emission, this option is not viable. Therefore, we used sky annuli in the range 12−30″ (100 μm) and 18−120″ (160 μm), depending on each specific source, with widths of the sky annulus ranging between 2−20″ (100 μm) and 3−30″ (160 μm). The flux errors were derived considering the local background rms and the values of the correlated noise derived for the DUNES program, which depend on the pixel size of the maps (in our case, 2″ for the 100 μm map and 3″ for the 160 μm map). To account for any other potential sources of error, including flux calibration and eventual aperture effects, we also included an empirical 10% error in quadrature. This is

[1] HIPE is a joint development by the *Herschel* Science Ground Segment Consortium, consisting of ESA, the NASA *Herschel* Science Center, and the HIFI, PACS, and SPIRE consortia.

[2] IRAF is distributed by the National Optical Astronomy Observatories, which are operated by the Association of Universities for Research in Astronomy, Inc., under cooperative agreement with the National Science Foundation.

Table 1. PACS 100 μm photometry.

Source ID	RA (J2000) (deg)	Dec (J2000) (deg)	Flux (Jy)	Comments
S CrA	285.285750	−36.955429	17.7 ± 2.6	SMM7 (Nutter et al. 2005)
CrA-466	285.32887	−36.97450	0.32 ± 0.05	G-113
#6	285.385710	−36.894553	0.34 ± 0.08	Chini et al. (2003), extended
G-85	285.390750	−36.962428	0.42 ± 0.06	Sicilia-Aguilar et al. (2008)
#8	285.409360	−36.890428	12 ± 2	Chini et al. (2003), extended
G-122	285.421760	−36.953843	0.61 ± 0.09	Sicilia-Aguilar et al. (2008)
G-65	285.417650	−36.862488	19 ± 3	Sicilia-Aguilar et al. (2008), mostly cloud emission
IRS 2	285.422790	−36.975106	82 ± 12	
IRS 2+ring	285.422790	−36.975106	104 ± 15	Including ring-like structure
HBC 677	285.423070	−36.997754	0.089 ± 0.014	
IRS 5a+b	285.450130	−36.955705	19.4 ± 2.8	Unresolved binary
FP-25	285.45193	−36.95413	15 ± 3	Probably extended, IRS 5 N
IRS 5ab + FP-25	285.450130	−36.955705	71 ± 10	Multiple system without spiral structure
IRS 5+spiral	285.450130	−36.955705	92 ± 13	Multiple system plus spiral structure
IRS 6a+b	285.459790	−36.943242	9.2 ± 1.3	Unresolved binary
V 710	285.46066	−36.96934	97 ± 14	SMM3 (Nutter et al. 2005), IRS 1
IRS 7w	285.47973	−36.95577	476 ± 69	Uncertain due to proximity of IRS 7e, FP-34
IRS 7e	285.48414	−36.95843	162 ± 24	Uncertain due to proximity of IRS 7w , FP-34
SMM 1A	285.48138	−36.961325	148 ± 22	Nutter et al. (2005), source #13 (Chini et al. 2003)
SMM 2	285.493130	−36.952151	12 ± 2	Nutter et al. (2005)
T CrA	285.494140	−36.963643	12 ± 2	
B185839.6-3658	285.50792	−36.899722	0.12 ± 0.03	BD candidate
CrA-159	285.637520	−36.972469	0.111 ± 0.016	
IRAS 18598	285.743990	−37.126549	52 ± 5	IRAS 18598
VV CrA	285.778000	−37.213581	80 ± 12	Extended?
CrA-45	285.816690	−37.235688	0.92 ± 0.13	YSO (Peterson et al. 2011)
R CrA	285.47343	−36.952274	71 ± 10	Strongly contaminated by IRS 7
SMM 1A s	285.47859	−36.97195	13 ± 2	Groppi et al. (2007)
#19	285.5521	−36.9544	0.72 ± 0.11	Chini et al. (2003), part of large cloud structure

Notes. Photometry of the known cluster members detected by *Herschel*/PACS at 100 μm. For extended sources, the photometry was obtained around the peak (or peaks), but the extended material results in a large uncertainty. In the "Comments" column we include the references of the source name and/or other naming conventions, and whether the source is extended or potentially contaminated.

Table 2. PACS 160 μm photometry.

Source ID	RA (J2000) (deg)	Dec (J2000) (deg)	Flux (Jy)	Comments
S CrA	285.285790	−36.955485	13.6 ± 2.7	
G-122	285.421180	−36.953821	2.2 ± 0.4	Sicilia-Aguilar et al. (2008)
IRS 2	285.422310	−36.974903	61 ± 12	
IRS 2+ring	285.422310	−36.974903	103 ± 20	Including ring-like structure
IRS 5a+b + FP-25	285.451320	−36.954874	23 ± 5	Multiple system without spiral structure
IRS 5a+b/FP-25 + spiral	285.451320	−36.954874	131 ± 26	Multiple system plus spiral structure
IRS 6a+b	285.460040	−36.943701	11 ± 2	
V 710	285.461110	−36.968953	70 ± 14	IRS 1, extended?
SMM 1A s	285.47914	−36.97314	30 ± 7	Groppi et al. (2007), extended?
IRS 7w+e	285.4812	−36.9564	880 ± 170	Binary plus surrounding structure
SMM 2	285.49313	−36.95201	25 ± 5	
T CrA	285.49493	−36.96386	13 ± 3	Uncertain due to proximity of IRS 7w/e
APEX 13+15	285.552040	−37.008617	0.46 ± 0.10	Sicilia-Aguilar (2011a), extended
APEX 6	285.577930	−37.023607	0.40 ± 0.08	Sicilia-Aguilar (2011a), extended
APEX 16	285.599610	−36.942940	0.28 ± 0.06	Sicilia-Aguilar (2011a), extended
APEX 19	285.635820	−37.033284	0.12 ± 0.03	Sicilia-Aguilar (2011a), extended
IRAS 18598	285.744070	−37.126434	42 ± 3	Extended?
APEX 7+10+24	285.770620	−37.242373	0.24 ± 0.05	Sicilia-Aguilar (2011a), extended
VV CrA	285.778020	−37.213602	66 ± 13	
CrA-45	285.816670	−37.235619	0.81 ± 0.16	Peterson et al. (2011)
#19 North	285.5520	−36.9549	13 ± 3	Part of source #19 from Chini et al. (2003), extended
#19 South	285.5646	−36.9631	2.4 ± 0.5	Part of source #19 from Chini et al. (2003), extended

Notes. Photometry of the known cluster members detected by *Herschel*/PACS at 160 μm. For extended sources, the photometry is obtained around the peak (or peaks), but the extended material results in a large uncertainty. In the "Comments" column we include the references of the source name and/or other naming conventions, and whether the source is extended or potentially contaminated.

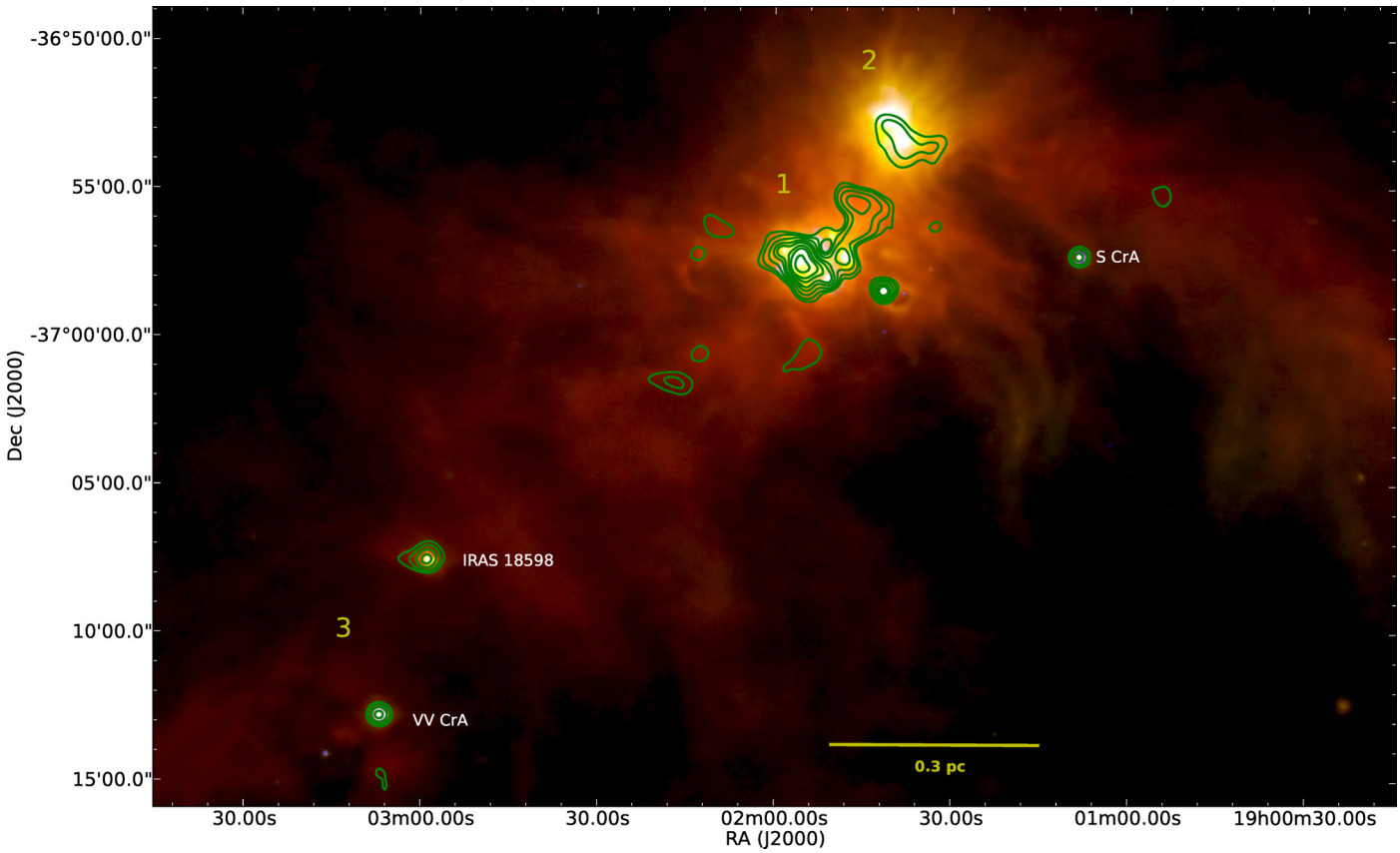

Fig. 1. Combined 3-color image (with MIPS/*Spitzer* 24 μm, *Herschel* PACS 100 and 160 μm as blue, green, and red, respectively) of the Coronet/CrA region, with the 870 μm LABOCA contours (at 0.1, 0.2, 0.4, 0.7, 1.0,1.5, 2.0,3.0,4.0,5.0, and 6.0 Jy/beam) in green (Sicilia-Aguilar et al. 2011a). To facilitate visual identification of the objects, we have labeled the prominent ones in white, and added yellow numbers to mark the three subclusters (Sect. 3), with 1 denoting the central cluster, 2 the northern subcluster, and 3 the southern subcluster.

the dominant source of error for bright sources, while the faint sources are dominated by the sky noise.

For the extended and relatively bright sources, we used the CLASS/GREG application from the GILDAS software package[3] to accurately select the emission structure, and to measure its flux and the corresponding sky. In this case, no aperture correction was used, and the errors were obtained in the same way as for the point-like sources[4]. The central part of the cluster (see Figs. 1 and 2) contains several very close, extended sources that are not easy to separate (e.g. IRS 7w/e, IRS 5a/b). The flux for these sources is thus uncertain, as we discuss when the individual sources are presented. There are several point-like sources that have some additional extended structure (e.g. IRS 2, the IRS 5 complex). To analyze the source spectral energy distribution (SED), we measured the compact part; the extended structure will be discussed separately. Some of the multiple sources are not resolved at all wavelengths. For instance, in the IRS 5 complex, containing IRS 5a, IRS 5b, and FP-25 (also known as IRS 5 N), IRS 5a/b are blended, but FP-25 is resolved at 100 μm. The complex forms an elongated structure containing the three objects at 160 μm. IRS 7w/e are also resolved at 100 μm but not at 160 μm, and both objects are very close to (but not blended with) the candidate Class 0 object SMM 1 A. The brightness of all these sources ensures that they are all detected, but the substantial nebular extended emission around them and the nearby objects is the main source of error in their photometry.

In general, the *Herschel* data offer an excellent view of the cluster center, where *Spitzer* surveys suffered from saturation and artifacts caused by the very bright sources, and submillimeter/millimeter studies lack sufficient spatial resolution to separate the emission from individual sources. It also reveals substantial cloud structure where evidence for extended material was not conclusive at other wavelengths (Fig. 1).

2.2. Other data

To complete the study of the different sources, we used the available optical, IR, and millimeter data for the cluster members. The summary of all data for the sources is shown in Table 3. Optical photometry is available in Bibo et al. (1992) for the bright sources and in López-Martí et al. (2004) for the fainter members. Most of the IR *Spitzer* photometry was published in Sicilia-Aguilar et al. (2008) and Currie & Sicilia-Aguilar (2011), including several IRS spectra. Peterson et al. (2011) presented detailed *Spitzer* IRAC and MIPS photometry for several of the sources already mentioned previously in the literature, plus some new member candidates. Submillimeter/millimeter data are listed in Groppi et al. (2004, 2007), Nutter et al. (2005), Chini et al. (2003), and Peterson et al. (2011).

We also revised the archive *Spitzer*/MIPS 70 μm data (AOR 3664640) for all sources using smaller apertures and

[3] See http://www.iram.fr/IRAMFR/GILDAS/

[4] In case of isolated extended sources, the size of the selected area encloses all the emission. Nevertheless, in case of nearby/blended sources, part of the flux may be lost and some flux from nearby sources may be present, so the error estimates include the flux variations observed when modifying the selected contours.

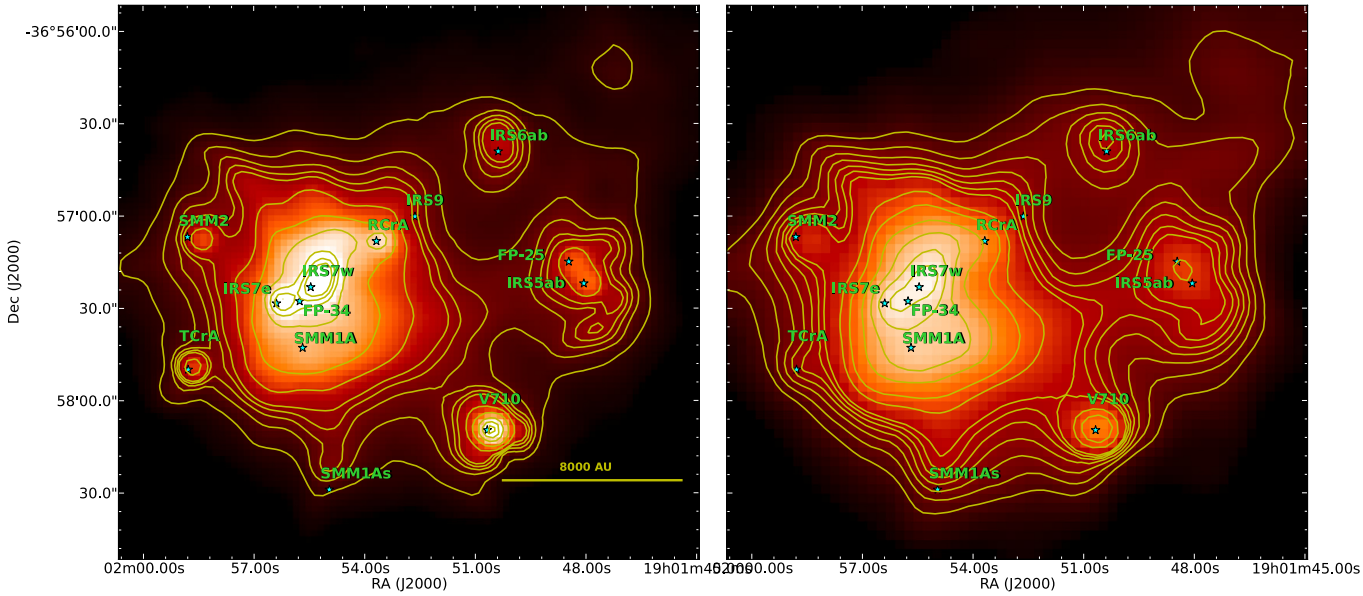

Fig. 2. Region around IRS 7w/e at 100 and 160 μm (*left* and *right*). Cyan stars mark the position of the known cluster members, labeled in green. The X-ray source FP-34 is situtated between the two far-IR peaks. IRS 7w is the brightest source in the field at both wavelengths, and it is clearly extended, although IRS 7e becomes increasingly bright at longer wavelengths. Both IRS 7w and IRS 7e are surrounded by a strongly emitting extended structure. The binary IRS 5 and the X-ray source FP-25 are surrounded by a distinct structure that could be a common filament or associated spiral arms. IRS 6 is an extended source. IRS 2 and V 710 are rather compact, albeit surrounded by extended structures. The contours mark the *Herschel*/PACS levels at 0.1, 0.15, 0.20, 0.25, 0.3, 0.5, 1, 2, 3, 4, and 5 Jy/beam (for the 100 μm image) and 0.4, 0.5, 0.6, 0.7, 0.8, 0.9, 1.0, 1.5, 2.0, 3, 4, 5, and 6 Jy/beam (for the 160 μm image).

improved aperture corrections, since some of the Sicilia-Aguilar et al. (2008) fluxes at 70 μm were higher than expected considering the MIPS 24 μm point and the *Herschel* data (which strongly suggested contamination by nebular emission). On the other hand, the 70 μm fluxes of many of the objects listed in Peterson et al. (2011) are lower than expected from the 24 and 100 μm fluxes. A significant problem for the *Spitzer* 70 μm photometry is that the field presents zones of substantial nebular emission, plus ghosts produced by the bright objects in the field, and moreover there is a non-negligible part of the flux at distances of 100″ (aperture correction of 1.10 for an annulus of 100″ radius, according to the MIPS manual). We therefore followed different procedures depending on the background of each object. For faint objects in the proximity of other sources or ghosts, we used a small aperture of 14.2″ (sky annulus 16−26.5″) with a large aperture correction (2.79). For isolated sources, we used a 40.4″ aperture with a 1.27 aperture correction and sky annulus 152−168″. These aperture corrections were obtained for isolated, known young stellar objects (YSO) in the field to avoid contamination by cloud material, and to minimize the temperature dependence of the aperture correction. For objects in crowded fields, the sky annulus had to be set to avoid the nearby emission from other sources, with the problem that there is non-negligible emission from the object at these close distances. Nevertheless, for faint objects the background emission and standard deviation usually dominate over the object flux at 16−26.5″. This results in a typical uncertainty of about 10%, which exceeds the uncertainties derived from calibration and background subtraction. For the final fluxes, we used the zeropoint in the MIPS manual (0.778 ± 0.012 Jy).

3. *Herschel* view of the CrA members

In this section, we describe the most important sources in the region related to known YSOs, as seen from the *Herschel*/PACS observations. We focus the discussion on objects that are known to be young cluster members from optical, X-ray, *Spitzer*, and submillimeter studies (see references in the introduction and Sect. 2.2). In addition to these objects, we have found several other sources in the mapped region that have not previously been classified as YSOs in the literature as well as some extended galaxies. Some of the new PACS sources may be extragalactic objects because their positions appear unrelated to other cloud emission. Conversely, a number of other sources are spatially coincident to the more general cloud emission, so they could be candidate members (either TTS or protostars), but the lack of more data on them does not allow us to unambiguously determine their cluster membership. These sources will be discussed in a follow-up publication of the Gould Belt Survey group.

The *Herschel* PACS data present a new view of the CrA star-forming region (Fig. 1). The emission at 100 and 160 μm follows our previous APEX/LABOCA observations at 870 μm well (Sicilia-Aguilar et al. 2011a), but the much higher spatial resolution and sensitivity of *Herschel* reveals several new interesting structures. As in the APEX/LABOCA data, the brightest part of the cloud is associated with the surroundings of the embedded sources IRS 7w and SMM 1 A (see Figs. 1 and 2). This also agrees with the results of Chini et al. (2003) and Groppi et al. (2007). The brightest part of the cloud contains two subclusters, the first (and brightest) central cluster, containing IRS 7e/w, SMM 1 A/As, R CrA, T CrA, IRS 5, IRS 6, and V 710 (Fig. 2), and the second located to the north, around TY CrA and HD 176386, with G-65 (Fig. 3). A dark lane (at *Herschel* wavelengths), coincident with the source SMM 6 in Nutter et al. (2005) and with the secondary 870 μm peak in our LABOCA map (Sicilia-Aguilar et al. 2011a) is visible between these two groups (see Fig. 1). In the first subcluster, the emission peaks are clearly related to the embedded protostars (the IRS 7 and IRS 5 complexes, SMM 1 A/As, IRS 6, V 710; see Fig. 2). The peak in the second subcluster is not related to

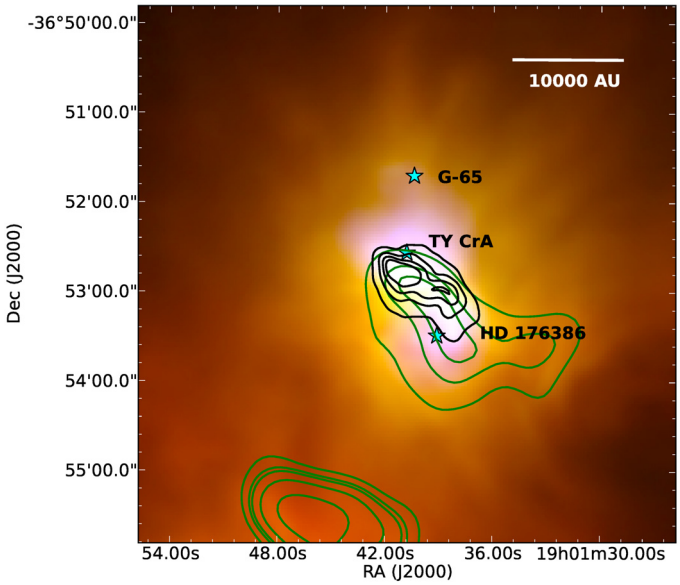

Fig. 3. Composite image (24, 100, and 160 μm) of the HD 176386/TY CrA region, with the LABOCA 870 μm contours (at 0.1, 0.2, 0.25, 0.4, and 0.7 Jy) marked in green, the 100 μm contours in black (at 0.4, 0.6, 0.8, and 1.0 Jy), and the positions of the sources as white stars. The 24 μm data trace the cavities cleared by the two massive stars. The 870 μm data reveal that the peak of the submm emission (and thus the expected higher mass column density) is located around HD 176386, but the star itself is not affected by high extinction. The *Herschel* data reveals a peak in the zone between the two mid-IR illuminated cavities, which could indicate the formation of condensations. To the south, some details of another submillimeter emission region that lacks far-IR sources can also be appreciated.

TY CrA or HD 176386, but is located between them. This is substantially different from the APEX/LABOCA observations, which showed a extended emission peaking at a position coincident with HD 176386, where the cloud density should be highest (Fig. 3).

In addition to the two subclusters, we also detected strong emission from several less-embedded, independent sources in the region (IRS 2, S CrA, G-85, CrA-159, CrA-466, among others), including a third subcluster to the south that is associated with several bright young objects (VV CrA, CrA-45, and IRAS 18 598) and some 870 μm extended emission (Sicilia-Aguilar et al. 2011a). Along with the individual YSOs, we detect extended cloud emission that covers the area where most of the known cluster members are located, including nebular emission associated with each subcluster, which is extended in the directions suggested by the Graham (1992) observations and the extinction maps by Kainulainen et al. (2009). Furthermore, we mention the occurrence of radial striations mainly visible in the *Herschel* emission blob that is associated with the HD176386/TY CrA region (Figs. 1 and 3). These might show an imprint of large-scale collapse motions or the accretion of additional material onto the central molecular clump, as seen for instance in the DR21 filament (Hennemann et al. 2012).

3.1. The IRS 7 complex

The brightest far-IR peak corresponds to the IRS 7 area (Fig. 2). IRS 7 is a binary embedded protostar, composed of IRS 7w (the brightest one at IR wavelengths) and IRS 7e. To the south of the two sources, we find the submillimeter source SMM 1 A (Nutter et al. 2005; Groppi et al. 2007). The PACS 100 μm data resolves all three peaks, but the 160 μm image shows an elongated structure with two peaks corresponding to IRS 7e/w, and a third emission structure related to SMM 1 A. Due to the difficulties to separate both objects from each other and from the extended cloud emission, the uncertainties in their fluxes are large (Table 3). The PACS positions of IRS 7w/e agree well with the MIPS 24 μm and *Chandra* X-ray positions. In addition, the X-ray emission source FP-34 (source number 34 of Forbrich & Preibisch 2007; see also Garmire & Garmire 2003) is located close to IRS 7e, but cannot be identified with IRS 7e itself (see also Peterson et al. 2011). FP-34 is as a single X-ray source located between the PACS emission peaks associated with IRS 7w, IRS 7e, and SMM 1 A. Although the bright emission in the region does not allow us to determine whether a fourth, fainter embedded object is present at the position of FP-34, it could also indicate that the X-ray emission is produced by other means (e.g. shocks; Favata et al. 2002) in the interface between IRS 7w and IRS 7e, or a jet related to the less-evolved SMM 1 A source. At least one Herbig Haro object in the region is known to be a source of X-ray emission (G-80; Sicilia-Aguilar et al. 2008).

The submillimeter source SMM 1A, identified by Nutter et al. (2005) as the brightest, most extended peak in the region, is detected by *Herschel* as a single peak at 100 μm, but appears as a bright, extended emission structure at 160 μm. This source and IRS 7 make up the brightest peak of our LABOCA observations, which could indicate a highly embedded source, or a region of very high dust density in the proximity of the known protostars. To the south of SMM 1A we detect another PACS source, identified as SMM 1As by Groppi et al. (2007) that has no *Spitzer* counterparts. Both sources are Class 0 candidates and are discussed in detail in Sect. 4.1.

3.2. IRS 2

The embedded IRS 2 source, classified as a Class I protostar with a spectral type K2 by Forbrich & Preibisch (2007), is one of the most interesting objects in the PACS data (Fig. 4). In the 100 and 160 μm images, it is consistent with a bright point-like source (with its three-lobe structure closely resembling the PACS PSF) in the rim of a ~5000 AU diameter ring- or bubble-like structure. The ring is clearly detected at the PACS wavelengths, but is not visible in the *Spitzer*/MIPS maps. At 870 μm, our LABOCA map shows the object to be slightly elongated in the direction of the ring, but the elongation is marginal considering the beam size of 19.2″ (Sicilia-Aguilar et al. 2011a). The best explanation is the presence of an envelope or cloud structure that is excavated by the (large opening-angle) stellar winds of IRS 2, that is asymmetric with respect to this object due to a non-uniform distribution of material (for instance, if IRS 2 were located at the edge of the cloud). There is no evidence of extended emission in the other direction. Despite the relative proximity of the bright V 710 source and the cloud emission, any potential structure to the east of IRS 2 with a brightness similar to the observed ring should be clearly identifiable and resolved.

3.3. The IRS 5 complex

Next to IRS 2, the binary pair IRS 5a/b and the nearby X-ray source FP-25 (source number 25 from Forbrich & Preibisch 2007, also known as IRS 5N; Peterson et al. 2011) offer the next interesting structure resolved in the *Herschel*/PACS maps (Fig. 2). The two components, IRS 5a and IRS 5b, with a

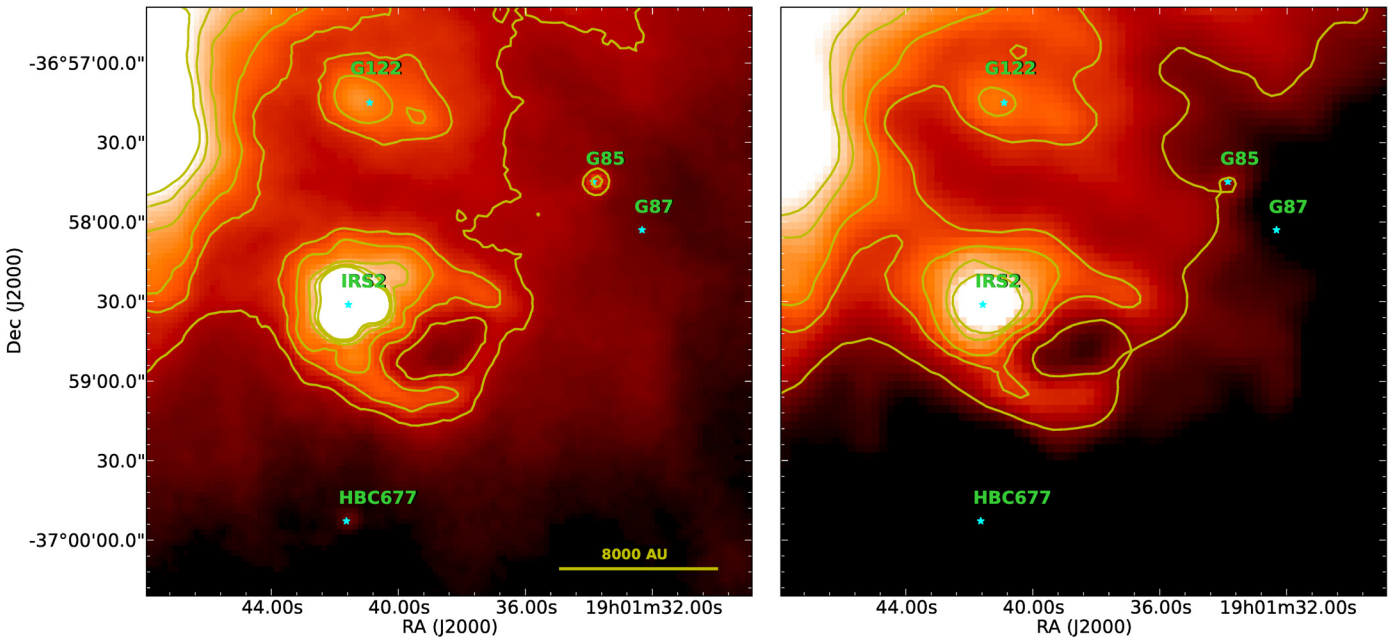

Fig. 4. Region around IRS 2 at 100 and 160 μm (*left* and *right*, respectively). Stars mark the location of known cluster members, labeled in green. G-85 and HBC 677 are clearly detected at 100 μm, but G-85 is only a marginal detection at 160 μm. Two small condensations to the north of IRS 2 are also apparent. The brightest one corresponds to G-122. The diameter of the IRS 2 ring is 27″, corresponding to about 4600 AU. The condensations are about 10″ in radius, or a diameter of ~3500 AU at 170 pc. Another disked object in the region, G-87, is not detected in either image.

projected separation of 78 AU for a distance of 130 pc (Nisini et al. 2005), are not resolved. FP-25 and IRS 5a/b are surrounded by substantial extended emission, in particular, a common filamentary structure that resembles a two-arm spiral with a resolved size corresponding to ~4000 AU, considering a distance of 138 pc. The extended structure is not detected in the *Spitzer* maps, but it is consistently detected in the two PACS filters and follows the contours in our 870 μm LABOCA maps. IRS 5a/b dominates the *Spitzer* and PACS 100 μm maps, but the single peak observed at 160 μm is closer to FP-25, which could indicate that the latter is not much fainter, but more embedded than IRS 5a/b. Based on their *Spitzer* and SMA observations, Peterson et al. (2011) classified FP-25 as a Class I object, which is also consistent with our *Herschel* observations. The shape of the spiral structure around the system is very similar to the ring detected around the young binary star SVS20 (which has a size of ~6800×4000 AU; Eiroa et al. 1997) and to the predictions for binary formation (Bate 2000; Kley & Burkert 2000), although the size of the spiral arms around the IRS 5 complex is about seven times larger than in Bate's simulation. The initial size and mass of the cloud, the initial angular momentum, and the binary separation are important parameters in determining the final structure. The projected separation between IRS 5a/b and FP-25 is approximately 800 AU (instead of 60−100 AU as in Bate et al. 2000), which would imply that the structure of the system is more affected by the properties of the surrounding cloud and directly dependent on the initial angular momentum (Bate et al. 2000) and, in general, on the initial conditions (Kley & Burkert 2000). Therefore, the observations of a larger spiral structure are in principle consistent with the results of hydrodynamical simulations. Nevertheless, the scale of the structure and the substantial cloud material around the sources do not exclude a complex, non-spherical structure like those that have been observed associated to the envelopes of some Class 0/I objects (Stutz et al. 2009; Tobin et al. 2011) or even heated material swept up by the jets or winds of the embedded protostars, similar to what is seen near IRS 2.

3.4. Other Class I candidates within the central cluster: IRS 6, V 710, and SMM 2

IRS 6 has been identified as a binary with a projected separation slightly larger than IRS 5a/b (97 AU for a distance 130 pc; Nisini et al. 2005), but the pair is not resolved with *Herschel*/PACS. The source is a relatively faint (compared to the rest of protostellar candidates in the region) and extended source (Fig. 2). In contrast to IRS 5 and IRS 2, the central emission is extended but there is no evidence for additional structures like extended rings or filaments or a compact core. The lack of an emission peak and its SED suggests that the *Herschel* emission is consistent with an extended envelope around the protostars, maybe a common envelope for both IRS 6 components.

V 710 (Fig. 2) has been classified as a K5-M0 Class I protostar (Forbrich & Preibisch 2007). At PACS wavelengths, it appears as a point-like, bright object near the IRS 7/IRS 5 complex. It is surrounded by strong extended emission associated with the central part of the cluster, although the object is bright enough to be clearly distinguished. The SED of the object (Fig. 5) is consistent with an embedded protostar, with a peak suggestive of temperatures between 500 and 100 K.

SMM 2, detected by Nutter et al. (2005) at SCUBA wavelengths (450 and 850 μm) and by Peterson et al. (2011) at 1.3 mm is also seen as an independent source in our *Herschel* maps (Fig. 2). It is also marginally detected at IRAC wavelengths, well-detected at MIPS 24 μm, and very bright at MIPS 70 μm. The *Herschel* detection is point-like, although surrounded by substantial extended emission. The SED is consistent with an embedded protostar, although the high fluxes measured at PACS wavelengths could indicate contamination by the surrounding cloud.

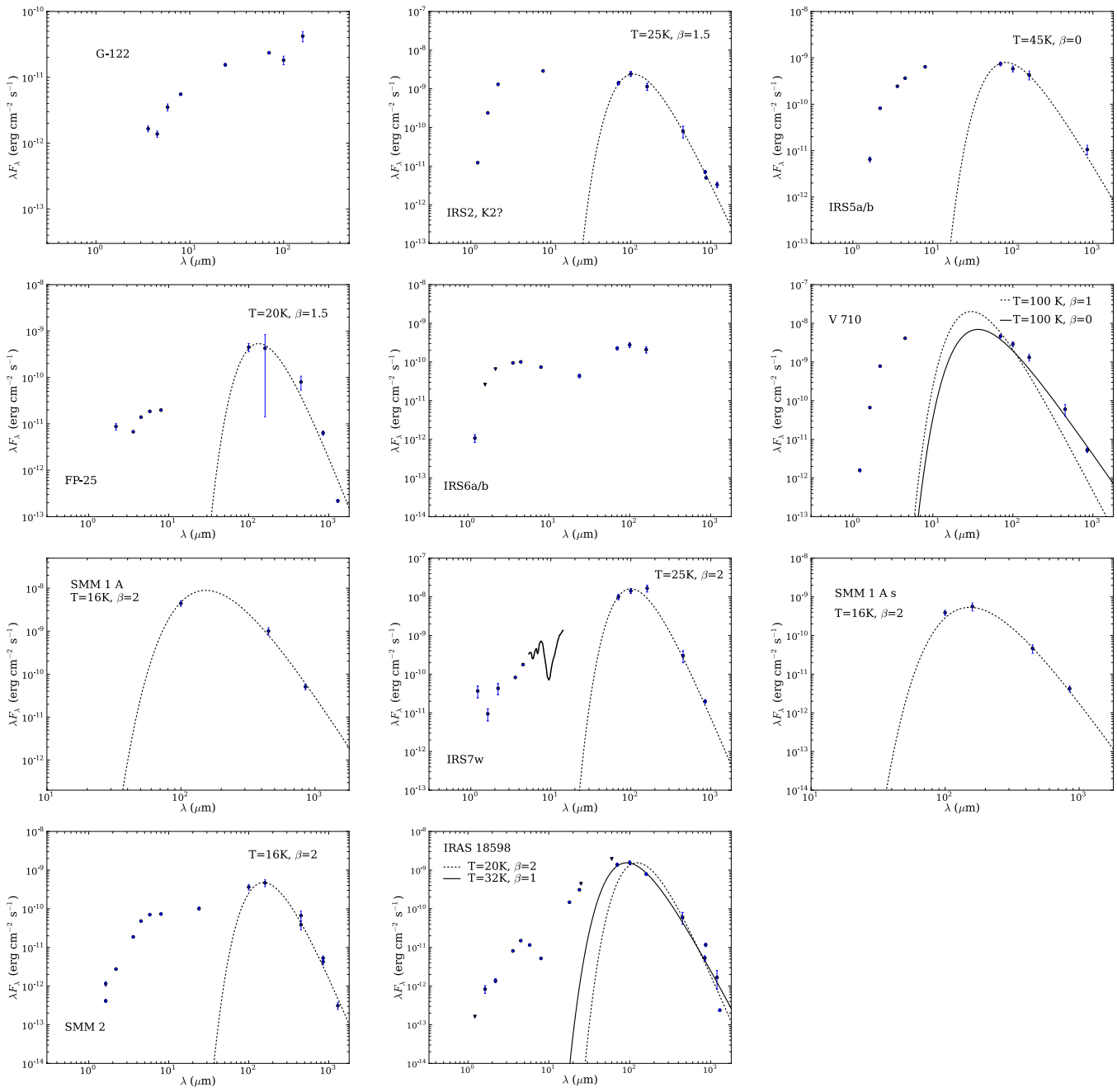

Fig. 5. SEDs of protostar candidates. Photometry detections are marked as circles, with upper limits marked as inverted triangles. The spectra correspond to *Spitzer*/IRS observations, when available. See Table 3 for details and references regarding the photometry data. In the relevant cases, a modified black-body is fitted to the data (as a whole for SMM 1 A and SMM 1 As; in the submillimeter range only for the other sources) and the corresponding values of temperature (T) and β are indicated in the figure, see Sect. 4.1 for more details. IRAS 18598 is probably composed of two sources.

3.5. Very low-mass Class I objects: G-122 and nearby condensation

The PACS data reveal two compact condensations to the north of IRS 2 (Fig. 4). One of them is associated with the X-ray source G-122, classified by Sicilia-Aguilar et al. (2008) as a probable Class I protostar. The other one is marginally detected at 100 μm, but becomes brighter at 160 μm. Both sources are extended, with approximate sizes of about 1600 AU at 138 pc. Because of the extended cloud emission, the photometry of the faintest source is uncertain, but G-122 is clearly detected with PACS. Combining *Spitzer* data, G-122 is consistent with a cold condensation that could correspond to a very low-mass Class I protostar (see Fig. 5). The nearby faint object is not detected at any *Spitzer* wavelengths, but the similarities with G-122 could indicate that it is another (fainter) very low-mass protostar. The projected separation between the centers of the two objects is ~26″ or about 3600 AU at 138 pc.

3.6. Solar- and intermediate-mass disked stars: S CrA, R CrA, and T CrA

The binary source S CrA is a bright object at PACS wavelengths (see Fig. 1). The source is relatively compact, but differences of 10−20% of the flux depending on the aperture selection suggest

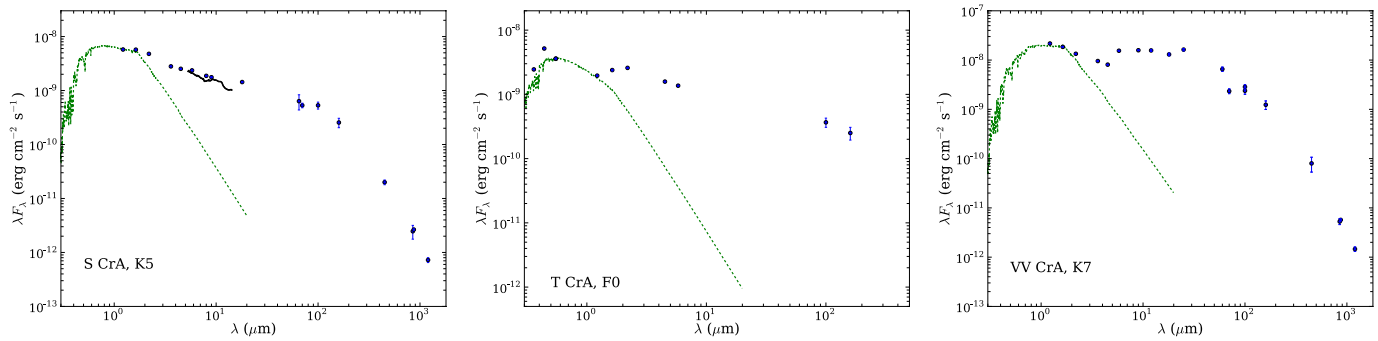

Fig. 6. SEDs of detected intermediate-mass stars and solar-type TTS. Photometry detections are marked as circles, with upper limits marked as inverted triangles. The spectra correspond to *Spitzer*/IRS observations, when available. See Table 3 for details of the photometry data. For comparison, a photospheric MARCS model (Gutafsson et al. 2008) with a similar spectral type is shown for each object (dotted line).

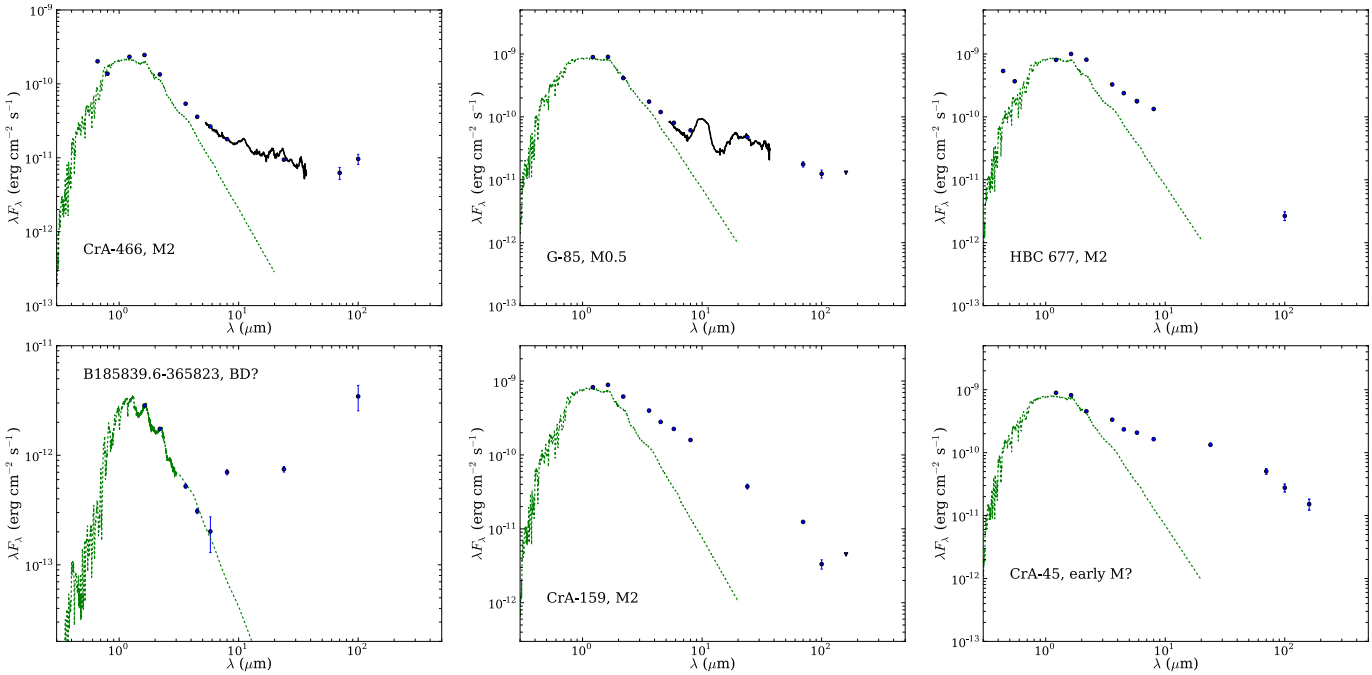

Fig. 7. SEDs of detected low-mass TTS. Photometry detections are marked as circles, with upper limits marked as inverted triangles. The spectra correspond to *Spitzer*/IRS observations, when available. For comparison, a photospheric MARCS model (Gutafsson et al. 2008) with a similar spectral type is shown for each object (dotted line). See Table 3 for details of the photometry data.

that it could be surrounded by some extended material, either of cloud or envelope origin. Its very complete SED (including optical, IR, and millimeter/submillimeter data) reveals a very massive and flared disk. Disagreement in the near- and mid-IR fluxes between the IRAC/MIPS and IRS data suggest that the short-wavelength emission could be variable, as has been seen in other actively accreting young sources.

R CrA (spectral type A5; Bibo et al. 1992) and T CrA (spectral type F0; Acke & van den Ancker 2004) are the two intermediate-mass stars with disks in the densest part of the cluster (see Fig. 2). They are both clearly detected in the PACS images, although the strength of the nearby sources (especially the IRS 7 complex and the extended cloud structure) make it hard to quantify their fluxes. In particular, the measured flux for R CrA is evidently contaminated by the nearby objects and cannot be used to constrain its disk properties. T CrA, which is more distant from the main emission peaks, is measurable within reasonable limits. Its SED is consistent with the presence of a flared, massive disk, and agrees with the spectral type of F0 and extinction $A_V = 2.45$ mag derived by Acke & van den Ancker (2004). The error in the flux at 160 μm is nevertheless large because of surrounding extended emission (Fig. 6).

3.7. Low-mass CTTS: G-85, CrA-466 (G-113), CrA-159, HBC 677, and B18598.6-3658

A few of the low-mass CTTS in the Coronet cluster are detected in the PACS images (Fig. 7). The extincted M0.5 source G-85 (Sicilia-Aguilar et al. 2008, 2011a; Fig. 4) is well-detected at 100 μm, and marginally detected at 160 μm. The M2 star CrA-466 (also known as X-ray source G-113) is also detected in both PACS channels, although the 160 μm detection is marginal. Two more M2-type sources, CrA-159 and HBC 677, are clearly detected at 100 μm, but not in the 160 μm images (Fig. 4).

Some emission is detected toward the BD candidate B18598.6-3658 (Wilking et al. 1997; Forbrich & Preibisch 2007), although its SED is hard to interpret. Considering the near-IR data from Wilking et al. (1997), the extinction estimate from Forbrich & Preibisch (2007), and the *Spitzer* detections (Peterson et al. 2011), the SED is consistent with a late-M

(M5-M7) star or BD with a remarkably bright transition disk. More data (e.g. confirmation of its spectral type) are required to determine the true nature of the source. In particular, although the agreement between the PACS detection and the near-IR position of the source is excellent and it is fully consistent with point-like emission like the rest of detected low mass disks, contamination by nebular emission or potential background objects should be ruled out.

The SEDs of the four detected known members (G-85, CrA-466, CrA-159, and HBC 677), very complete thanks to the availability of optical and *Spitzer* data, reveal different types of protoplanetary disks. We discuss their disk morphologies in more detail in Sect. 4.2.

3.8. Northern subcluster: HD 176386, TY CrA, and G-65

The stars TY CrA (B8) and HD 176386 (B9) are multiple systems that lie to the north of the main star-forming region (Bibo et al. 1992). Both of them have been detected at optical and IR wavelengths, although the presence of substantial cloud material in the region has not unambiguously resolved the question of whether they have circumstellar disks. MIPS/*Spitzer* data reveal extended cloud emission, and a cavity-like structure presumably created by TY CrA. Since they do not have an excess in the near-IR, they are most likely diskless (Sicilia-Aguilar et al. 2011a; Currie & Sicilia-Aguilar 2011). The PACS images reveal substantial emission in the region, but unlike the MIPS image (that showed emission centered around each one of the objects) and the 870 μm LABOCA map (that revealed extended emission centered around HD 176386), the PACS data reveal an elongated structure located between the two optical stars (Fig. 3). There is no detectable emission (at least, not over the extended background emission) at the positions of the two stars. The extended emission is composed of a brighter, larger blob closer to TY CrA and to the edge of the MIPS cavity, and a weaker extended tail that coils toward HD 176386. The full structure is about 10 000 AU in size (for a distance of 138 pc), which could correspond to an embedded object or a heated clump located between the two intermediate-mass stars (see Fig. 3). We cannot fully exclude the possibility that an enhanced contribution from atomic lines (e.g., [CII] at 158 μm) to the total emission within the continuum filters can also play a role here. Some weaker emission is observed around the structure, in particular, toward the low-mass object G-65, although G-65 itself is not clearly detected due to the strong background gradient. The fact that the PACS source(s) are not detected at MIPS 24 μm (MIPS 70 μm shows extended emission in the area without differentiated peaks) suggests cold and dense material compressed by the winds of the two nearby optical stars. Such a structure, if dense enough, could be the ideal environment for a new small episode of triggered star formation.

3.9. Southern subcluster: VV CrA, IRAS 18598, and CrA-45

To the south of the main star-forming region, we find three bright objects, IRAS 18598, VV CrA, and CrA-45; see Fig. 1. IRAS 18 598 has some evidence of extended emission at PACS wavelengths, which is consistent with the extended structure observed at 870 μm (Sicilia-Aguilar et al. 2011a). Its SED is hard to interpret, since it probably includes a near-IR source that dominates the *Spitzer* IRAC/MIPS emission, plus an extended structure that is responsible for most of the far-IR and submillimeter emission. More observations are required to determine the nature of this object.

VV CrA is a known binary system with an IR companion (see the detailed modeling by Kruger et al. 2011). The optical object has been classified as K7 (SIMBAD; Bast et al. 2011). The PACS flux at 160 μm shows extended emission, which could be associated with remnant cloud material or to the envelope of the IR companion. Small differences in the measured flux at 100 μm that depend on the aperture suggest that the IR emission could be extended. Simple SED fitting, assuming that the optical companion is a K7 star, suggests that the extinction to the optical source is rather A_V = 15 mag, instead of the 26 mag suggested by Kruger et al. (2012), but further modeling of the SED is hindered by the dominant IR companion.

To the south/east of VV CrA we find the source CrA-45 (according to the IDs in Peterson et al. 2011; also known as 2MASS J19031609-3714080), which had been previously identified as a YSO candidate (Gutermuth et al. 2009). The object has been detected at *Spitzer* wavelengths, and its SED is consistent with a low-extinction, early-M type CTTS.

3.10. Other sources in the cluster

Source SMM 6 from Nutter et al. (2005), which is one of the strongest peaks in our LABOCA map (Sicilia-Aguilar et al. 2011a), shows very little emission at 160 μm and is darker than the surroundings at 100 μm, suggesting that it is a cold starless condensation. We discuss it in more detail in Sect. 4.1.

Source #19 from Chini et al. (2003) appears as a complex emitting structure in the *Herschel* images. It presents two relatively extended peaks (north and south in Table 2, which could simply be denser parts of the cloud), together with filamentary structures that seem to extend from the central peaks.

Finally, the extended emission seen with MIPS to the north/west of CrA-4111 is detected at PACS wavelengths as cloud emission with at least one, but probably up to three point sources. At 100 μm, only one of the sources is clearly resolved as an independent object (at 19:01:18.73, −37:02:60.7), while two more faint compact sources are resolved at 160 μm (at 19:01:19, −37:03:22 and 19:01:19, −37:02:51). Only the first of these is detected (marginally) in IRAC at 4.5 μm (which could indicate an outflow) and MIPS/24 μm. The association with extended cloud material and nearby YSO in all these cases makes them good candidates to be new embedded cluster members or very low-mass protostars, although the lack of more data does not allow us to rule out the possibility of extragalactic sources seen in projection against the cloud. The complete list of newly detected *Herschel* sources and their analysis will be presented in a follow-up publication by the Gould Belt Survey group.

3.11. Non-detected YSOs

Many of the disked TTS listed in the literature and some of the candidate protostars detected at X-ray (Forbrich & Preibisch 2007; Sicilia-Aguilar et al. 2008, 2011a; Currie & Sicilia-Aguilar 2011; Peterson et al. 2011) are not found in the PACS images. This is especially true of the faintest very low-mass objects and the objects with faint IR fluxes. The presence of emission from substantial cloud material does not allow to place reasonable upper limits in many cases (G-32, G-36, G-43, G-65, G-94, G-95, G-112, CrA-205, and CrA-4111). For objects located in clean areas, the PACS non-detections set important constraints on the properties of several sources (see Table 4).

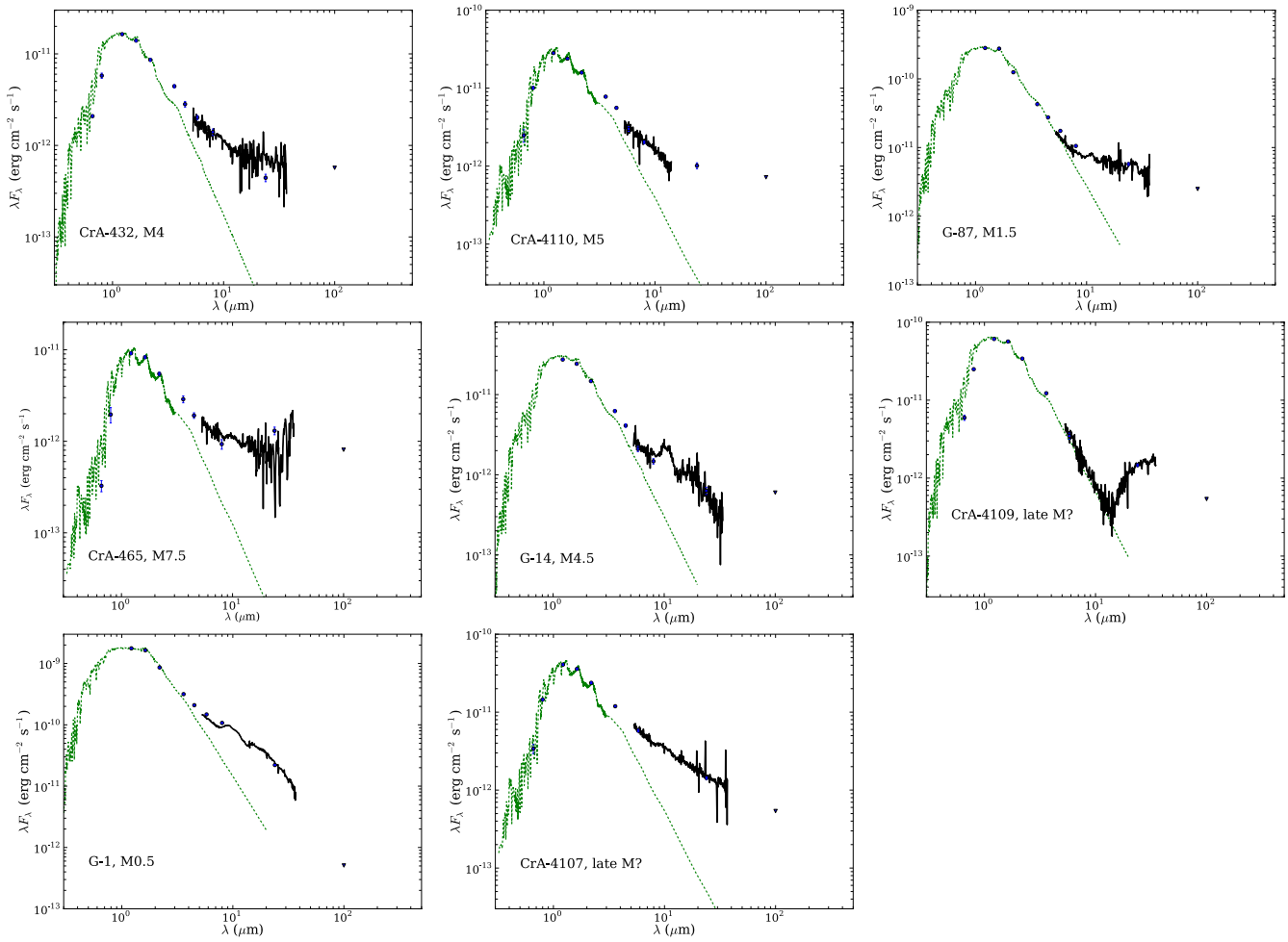

Fig. 8. SEDs of undetected low-mass TTS with stringent upper limits. Photometry detections are marked as circles, with upper limits marked as inverted triangles. The spectra correspond to *Spitzer*/IRS observations, when available. For comparison, a photospheric MARCS model (Gutafsson et al. 2008) with a similar spectral type is shown for each object (dotted line). See Table 3 for details regarding the photometry data.

Table 4. Upper limits for undetected objects.

Object	λ (μm)	Upper limit flux (Jy)	Comments
CrA-432	100	0.019	
CrA-4110	100	0.025	
G-87	100	0.082	Transitional disk
G-45	100	0.018	
CrA-465	100	0.027	
G-32	100	0.027	
G-14	100	0.020	
CrA-4109	100	0.018	Transitional disk
G-1	100	0.017	Dust-depleted
CrA-4107	100	0.018	
G-85[a]	160	0.69	Pre-transitional disk
CrA-159	160	0.24	Truncated disk?

Notes. Photometry 3σ upper limits for the objects with known IR excess not detected by PACS. Only objects with significantly low upper limits (compared to their mid-IR emission) are listed here. [(a)] G-85 is a marginal (2.5σ) detection at 160 μm, so we expect that although uncertain, its upper limit to the flux at this wavelength is relatively close to the real value.

Of the protostellar candidates detected at X-ray wavelengths, G-45 may possibly be a protostellar condensation, undetected in PACS because of surrounding cloud emission, although the scarcity of *Spitzer* data does not allow us to fit any model and more observations are desirable. Some extended emission is seen near the X-ray objects G-74 and G-128, although not at the same position. The X-ray emission could be related to potential very low-mass objects objects (similar to G-122), or to background extragalactic sources.

Of the undetected TTS, stringent upper limits can be placed for G-1 (also known as HBC 680, M0.5), G-14 (M4.5), G-87 (M1.5), CrA-4107, CrA-4109 (both probably late M stars), CrA-4110 (M5), and the BD candidate CrA-465 (M7.5; Fig. 8). Some diffuse emission is seen near HBC 679, but since this object did not show any excess emission at *Spitzer* wavelengths (Currie & Sicilia-Aguilar 2011), it is most likely of nebular origin. The upper limits of G-1 confirm a very low level of emission for this object in the far-IR, as has been inferred from *Spitzer* data, which makes it a candidate for hosting a globally dust-depleted disk (Currie & Sicilia-Aguilar 2011). The upper limits also place strong constraints on the disk of G-87, another candidate for a low dust-mass or dust depleted disk. The case of CrA-465 is more uncertain, since the MIPS images already suggest the presence of some nebular contamination, and the LABOCA map confirmed background extended emission, so the PACS data probably contain substantial cloud contamination. The detailed properties of these disks are discussed using simple disk models in Sect. 4.2.

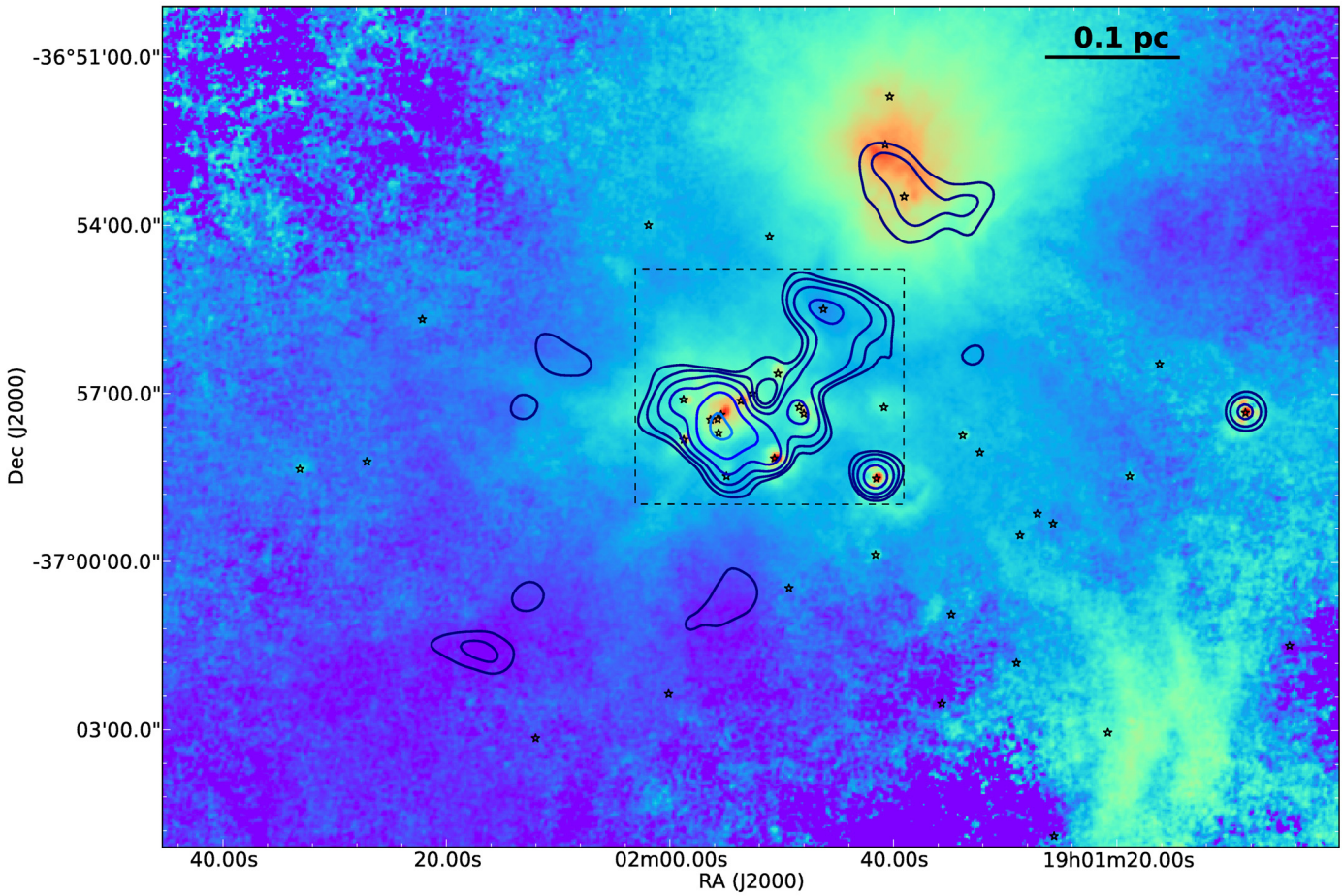

Fig. 9. Approximate temperature map, resulting from dividing the 100 μm by the 160 μm images. The known cluster members are marked as stars, and the LABOCA 870 μm contours at 0.1,0.2,0.4,0.8,1.6,3.2,6.4, and 12.8 Jy/beam are also displayed. The color gives an approximate idea of the temperature of the region, with red being the hottest (100 μm emission stronger than 160 μm emission) and violet denoting the coldest (160 μm emission stronger than the 100 μm emission). Protostars and disks tend to be hot (red), while the starless 870 μm regions are clearly colder than the rest of the cloud. The dashed-line box marks the region zoomed in in Fig. 10.

4. Analysis and discussion

4.1. Protostars, envelopes, and disks

To gain some insight into the mass and temperature of the objects detected by *Herschel*/PACS, we have constructed an approximate temperature map by dividing the 100 μm image by the 160 μm one (Fig. 9). This map provides important relative information on a pixel-by-pixel scale, which in turn is vital for characterizing the extended structures and the whole cloud, also in the regions without *Herschel* emission. Bright sources in the ratioed map correspond to objects with hotter temperatures, while cool regions that are stronger emitters at 160 μm than at 100 μm appear to be faint. With this exercise, we confirmed the existence of a cold, well-defined structure in the position of the submillimeter source SMM 6 (see Fig. 10), which is also coincident with an extended peak in the APEX/LABOCA 870 μm map, which is consistent with a relatively massive and cold core. Other structures detected at 870 μm that have no evident PACS counterparts are also consistent with cold regions (see Fig. 9), while the emission around HD 176386 and TY CrA appears to be hot, which indicates either heating by the nearby intermediate-mass stars or even the presence of some new embedded protostars. The differences between IRS 7w vs. IRS 7e and IRS 5a/b vs. FP-25 are also evident, with IRS 7w being hotter than IRS 7e, and IRS 5a/b being hotter than FP-25. Without additional data, however it is hard to establish whether this difference is due to evolution, viewing angle, or source mass. The very low-mass Class I candidate G-122 is also colder than typical, higher-mass Class I sources, and the Class 0 candidates SMM 1 A and SMM 1 As are also cold and probably extended.

By observing their SEDs (Figs. 5–8), the objects can be classified as protostellar Class I candidates (with SEDs peaking in the mid-IR and silicate features in absorption, when an IRS spectrum is available) or Class II sources with disks (with SEDs peaking in the optical or near-IR and silicate features in emission). Objects detected only at far-IR/submillimeter wavelengths are Class 0 candidates. In principle, our *Herschel* data confirm the previous classification in the literature, with objects such as IRS 7w, IRS 5, V 710, and SMM 2 being Class I candidates, while S CrA, T CrA, G-85, CrA-159, and similar sources are Class II objects. A few objects have an uncertain nature (e.g. IRS 2), and in other cases, the far-IR detection is probably associated with nearby cloud material (e.g. HD 17 6386), remnant envelopes, or a embedded nearby companion (e.g. IRAS 18 598).

To obtain more precise results, we explored different types of diagnostic diagrams involving the MIPS 24 and 70 μm data and the PACS photometry for the detected objects and those with relevant upper limits (Fig. 11), confirming this classification. The main parameter that affects the flux ratios is the object temperature. While disks are relatively flat or with a moderate negative

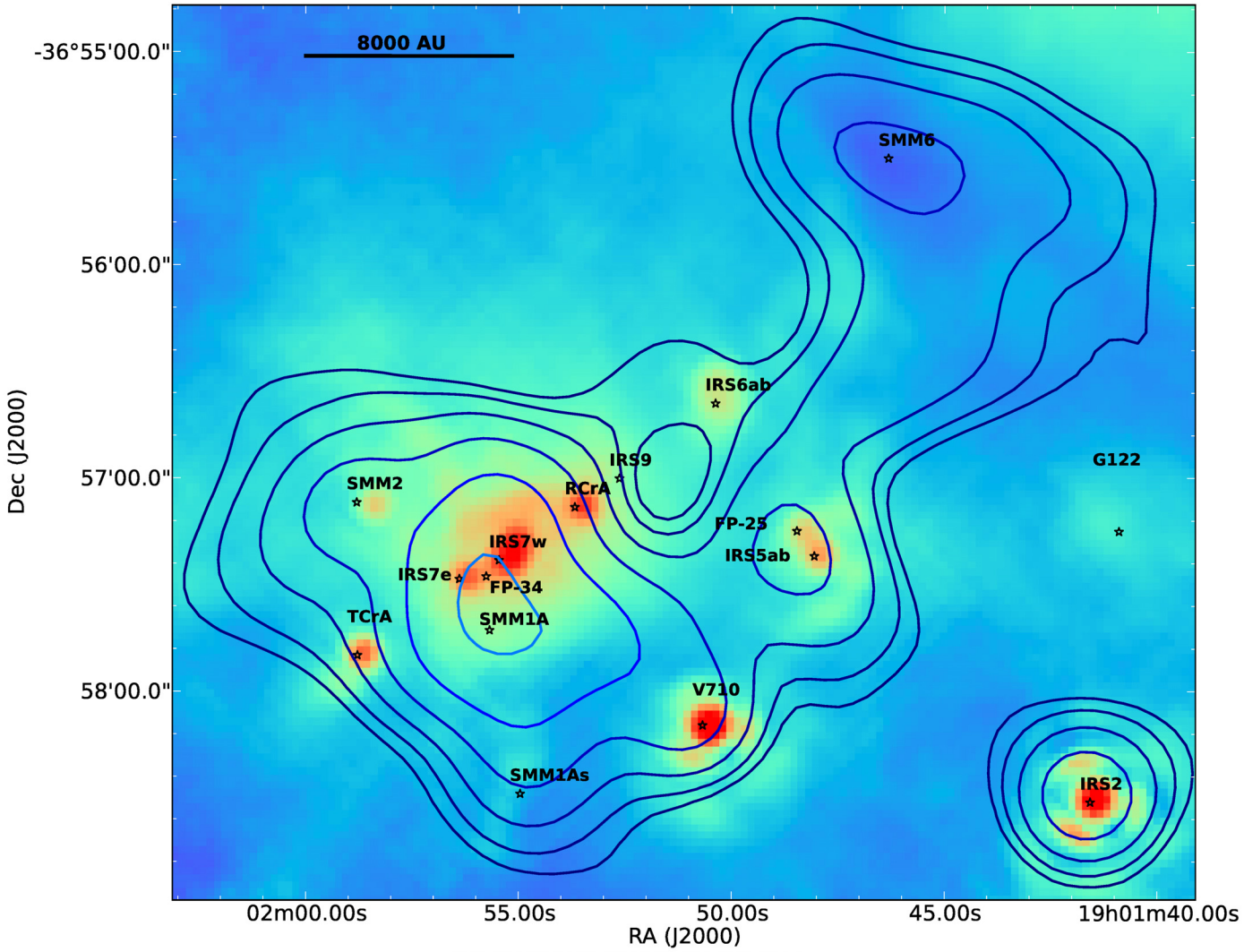

Fig. 10. Expanded view of the approximate temperature map from Fig. 9. The known cluster members and submillimeter emission regions are marked by stars and labeled. Protostars and disks are hot (red), while the starless 870 μm regions are clearly colder than the rest of the cloud. FP-25 is colder than IRS 5, and IRS 7e is also colder than IRS 7w. There is no significant emission near IRS 9, located to the east of a submillimeter "hole". The Class 0 candidates, SMM 1 A and SMM 1 As, are clearly colder than the dominant Class I protostars and the disked objects. The very low-mass protostellar candidate, G-122, is also colder than more massive Class I sources. The secondary peak of the LABOCA map, coincident with source SMM 6 from Nutter et al. (2005), is a distinct region even colder than the Class 0 protostars.

slope in the 24−70−100−160 μm range, protostellar objects can show flat, rising, or decreasing slopes in this range, depending on their temperatures. The second important parameter is the object mass. Massive disks have much flatter slopes than depleted disks, which becomes clear in the relation between the 24 μm and 100 μm flux (see the loci of the typical disks such as G-85, CrA-45, CrA-466 vs. that of the mass-depleted or low mass disks such as CrA-159 and G-1). Dust-depleted disks would also have a higher 24 μm/160 μm ratio, although none is detected at this wavelength. The masses, temperatures, and evolutionary state of protostellar objects are to some extent degenerate and difficult to uniquely determine without detailed modeling, although the general trend is that less massive and less evolved objects will tend to have lower fluxes and lower temperatures (Myers & Ladd 1993). The distinction between protostars and disks is thus maximal in the diagrams that include the shorter wavelengths (24 μm). The 100 μm/160 μm vs. 100 μm diagram is harder to interpret in terms of evolutionary state, since emission at these wavelengths in both protostars and disks comes mostly from small cold grains, which means that objects are separated by their luminosity. The low-mass protostar candidate G-122 is found in an intermediate location due to its low flux and long wavelength SED peak (low temperature). Although there are fewer objects detected at 70 and 160 μm (in particular, among the low-mass protostars and low dust-mass disks), these diagrams also reveal a similar trend.

The PACS and submillimeter data for two of the sources associated with the main cluster (SMM 1 A and SMM 1 As; Groppi et al. 2007) strongly resemble the emission expected for Class 0 objects. SMM 1 A has already been classified as a potential Class 0 source (Nutter et al. 2005). Including the *Herschel* data, we constructed simple modified black-body models for these objects, following Ward-Thompson et al. (2002). The emission of a modified black-body, or gray-body, can be written as

$$F_\nu = B_\nu(T)(1 - e^{-\tau_\nu})\Omega, \quad (1)$$

where F_ν is the flux density, $B_\nu(T)$ is the black-body emission for a temperature T, τ_ν is the frequency-dependent optical depth, and Ω is the solid angle subtended by the source. If we assume

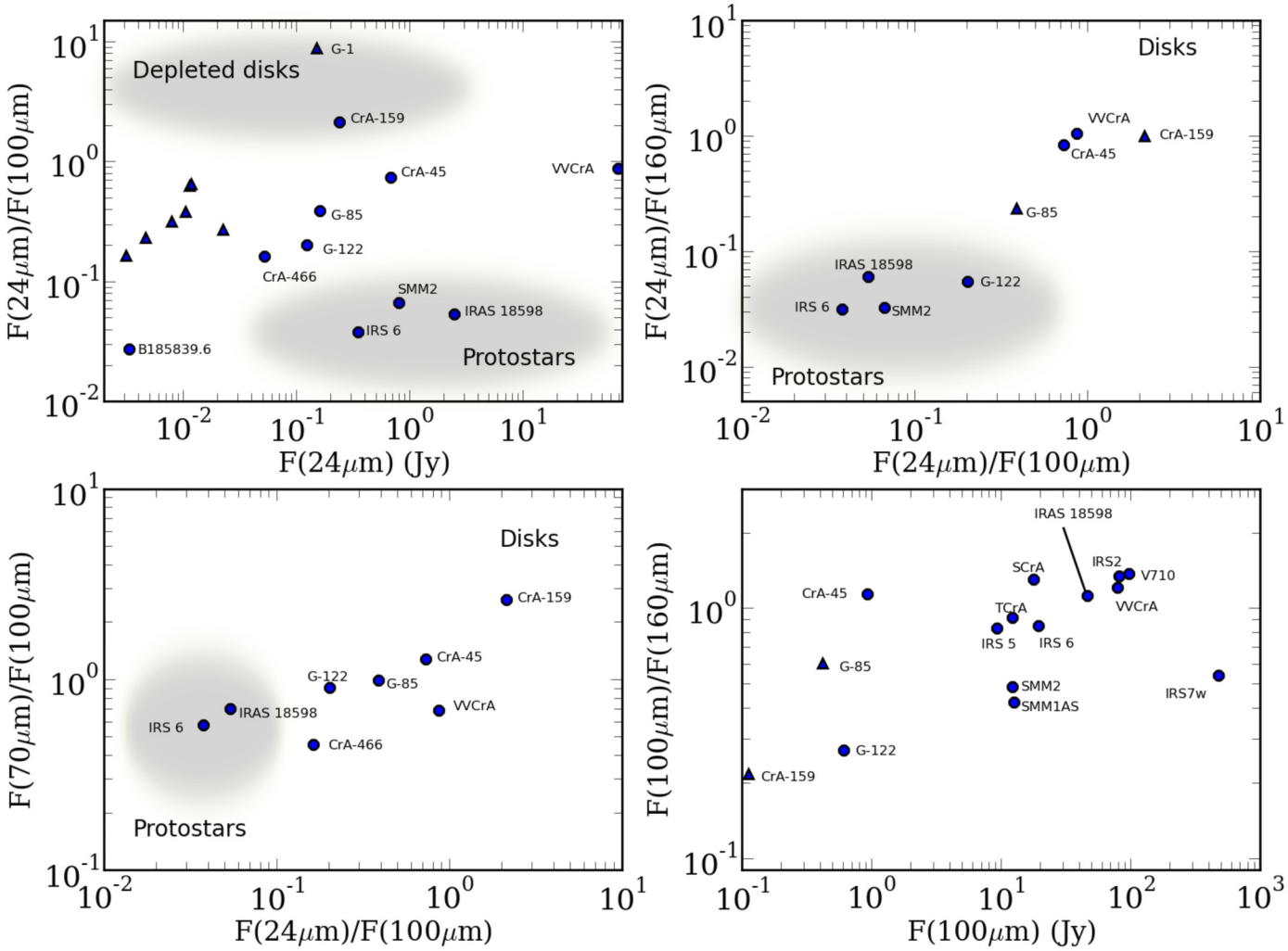

Fig. 11. Different fluxes and flux ratios for the CrA members. Lower limits in the ratios (for the cases with upper limits in the *Herschel*/PACS fluxes) are displayed as triangles. Approximate regions for depleted disks, disks, and protostars are marked. The emission of IRAS 18 598 is dominated by the far-IR counterpart.

that at long wavelengths the optical depth follows a power law with frequency, $\tau_\nu \propto \nu^\beta$, it is possible to derive the temperature of the source. Taking the values from Ward-Thompson et al. (2002) for $\beta = 2$ and $\tau_{200\,\mu m} = 0.06$, we obtain very good fits to both objects for temperatures around 16 K (see Fig. 5), consistent with pre-stellar cores. Nevertheless, more data, including higher resolution maps, are required to fully determine the nature of these objects, since external heating may also play a role, especially in the surroundings of other bright protostars (Lindberg & Jørgensen 2012).

As a comparison, and although a modified black-body does not provide a good fit to any of the remaining protostars, we repeated this exercise for the submillimeter part of the SEDs of the Class I objects with enough long-wavelength data (see Table 5). The fits are also displayed in Fig. 5 together with the temperature and β coefficient information. Except for SMM 2, which is adequately reproduced at long wavelengths with a similar model to SMM 1 A and SMM 1 As, all other objects require higher temperatures (in the range of 20−100 K) and different frequency power law exponents ($\beta = 0$−2). If we identify this longer wavelength part of the SED as the remaining envelope material of the source, this would suggest higher temperatures and different degrees of grain growth, as expected if these objects are more evolved than the Class 0 candidates.

4.2. Disk properties in the Coronet cluster

Although the Coronet cluster is a very young region (1−2 Myr; Sicilia-Aguilar et al. 2011a) and its compactness suggests a small age spread among the cluster members, we observe all types of protoplanetary disks among the solar-type and low-mass stars (see Figs. 6 and 7). To explore the disk structure of the objects, we modeled their SEDs using the RADMC 2D code (Dullemond & Dominik 2004). The RADMC code allows us to construct disk models to reproduce the SEDs of the different objects, using the observed stellar parameters to determine the luminosity (effective temperature $T_{\rm eff}$, stellar radius R_*) and varying the disk mass, radius, and vertical scale height. The disks are assumed to be flared with a single flaring law at all radii, $H_{\rm p}/R \propto R^{1/7}$, and the vertical scale height at the disk outer radius, $H_{\rm rdisk}/R_{\rm disk}$, is varied to fit the data. We assumed an inner disk rim at the dust destruction radius (for silicate dust, located at the distance at which the temperature reaches 1500 K), and a typical grain population with sizes between 0.1 and 100 μm

Table 5. Temperature and luminosity for the protostellar candidates.

Object	Class	T (K)	β	L_{bol} ($L_\odot$)	Comments
G-122	I/0:	–	–	0.005:	No submillimeter data
IRS 2	I	25	1.5	0.8	
IRS 5a/b	I	45	0	0.2	
FP-25	I	20	1.5	0.05:	Contamination by IRS 5a/b
IRS 6a/b	I	–	–	0.04:	No submillimeter data
V 710	I	100	0/1	3.1	
SMM 1 A	0	16	2	0.5	
IRS 7w	I	25	2	0.9	
SMM 1 As	0	16	2	0.04	
SMM 2	I	16	2	0.04	
IRAS 18598	I	20/32	1/2	0.3	

Notes. Temperature, frequency exponent, and bolometric luminosity for the sources considered as Class 0 and Class I protostars. For Class I objects, T and β refer to the fit to the longer wavelengths, which can be assimilated to the envelope/outer disk, while the luminosity is in all cases the integrated bolometric luminosity derived from the full SED, without applying additional corrections. The luminosity integration was performed assuming that the object can be reproduced by a sum of black-bodies with different temperatures to extrapolate the emission at longer and shorter wavelengths. Typical errors are in the range 10−20%. More uncertain values (usually due to the uncertainty of the photometry and/or to the lack of observations at longer wavelengths) are marked by ":". The envelope temperature of G-122 and IRS 6a/b cannot be determined because of the lack of submillimeter data, while the long wavelength SEDs of V 710 and IRAS 18598 can be fitted with different values of T and β.

following a collisional power law distribution with exponent −3.5. We took the outer disk radius to be 100 AU for the low-mass stars and 300−400 AU for the intermediate-mass stars[5]. The dust component of the disk was assumed to be composed of amorphous grains with similar amounts of Mg and Fe (Jäger et al. 1994; Dorschner et al. 1995[6]). This simple dust model reproduces the strength of the silicate features very well, although we note that the main purpose of this exercise is to understand the global SED shape, and not the dust composition in the disk atmosphere. In addition, 25% of carbon was included, with a similar size distribution as for the silicate grains. To obtain the full disk mass, we considered a gas-to-dust ratio of 100. We assumed that the dust temperature does not depend on the grain size, and the dust grains were considered to be well-mixed (i.e., without size-dependent differential settling). The stellar parameters (R_* and T_{eff}) were estimated from the temperature-spectral type relation for Taurus stars (Kenyon & Hartmann 1995), and we varied the stellar radius to reproduce the total observed luminosity in the optical/near-IR.

These simple models do not account for the many effects expected in protoplanetary disks (e.g. differential settling and grain growth, inside-out evolution), but our aim is to understand the global SED shape and properties of the disks. Only when no reasonable fit to the observed SED could be achieved with the simplified models, we included additional parameters, specifically by considering inclusion of large grains/removal of small grains in the dust component, modification of the inner disk rim to include an inner hole at distances larger than the dust destruction radius, and variation of the flaring and dust properties between the inner and outer disk. This is the same procedure as the one we followed for the disks in Cep OB2 (Sicilia-Aguilar et al. 2011b). The properties of the best-fitting models are listed in Table 6. The models are displayed in Fig. 12. We did not attempt to model objects that are problematic due to companions (VV CrA; Kruger et al. 2011) or nebular emission (HD 176386), since these simple disks models would not be adequate.

Several of the disks could be well-fitted with models that reproduce the typical behavior of CTTS disks: relatively massive, flared disks with a vertical scale height similar to that expected from hydrostatic equilibrium, which suggests little dust settling. They include the most massive members (T CrA and S CrA) and CrA-45 and CrA-466 of the lower-mass stars, although the high excess at 2−8 μm observed in S CrA and T CrA suggests the presence of a slightly puffed-up inner rim and the mid-IR emission of CrA-466 suggests some settling (or a departure from hydrostatic equilibrium) or inside-out evolution. The fit of CrA-45 is uncertain because its spectral type and extinction are unknown, and the mismatches between the 2MASS, IRAC, and MIPS fluxes suggest some degree of IR variability. Even though all these four disks are relatively massive, only the disk around S CrA exceeded the minimum mass for the solar nebula (Weidenschilling 1977), always assuming a standard gas-to-dust ratio of 100. The model fits also proved that, although far-IR and submillimeter data are needed to determine the disk mass correctly, the 30 μm IRS data already put very strong constraints on the amount of dust. For the object with the most complete submillimeter data (S CrA), the SED shape suggests grain growth up to millimeter-sized grains. A good fit is attained using a dust distribution with sizes 0.1−10 000 μm and a collisional power law distribution with exponent −3.5.

The *Herschel* observations reveal some severely mass-depleted disks, with disk masses below 10^{-5} M_* derived from the *Herschel* data and the best-fit models, and considering a standard gas-to-dust ratio (100): CrA-159, HBC 677, and G-1.

The most remarkable case is CrA-159. While it has relatively flared and optically thick disk with a large vertical scale height and strong near-IR excess, the very low PACS flux can only be reproduced assuming a very low dust mass. A good fit is achieved assuming that the disk is truncated to about 40−50 AU. A modification of the grain distribution (for instance, reducing the amount of >20 μm grains; see dashed line for CrA-159 in Fig. 12) can explain the low PACS fluxes but still results in too high 24 μm fluxes. The fact that the 24 μm flux is lower than expected even for a truncated/low-mass model could be a sign of a gap, albeit at a larger radius than in typical pre-transitional disks (Espaillat et al. 2010). A large gap could help to reduce the mid-IR flux without changing the grain size distribution and

[5] S CrA and T CrA. In both cases we started with a 100 AU outer disk radius, but the submillimeter and millimeter observations of S CrA suggest a slightly larger radius and the presence of larger dust grains.

[6] See http://www.astro.uni-jena.de/Laboratory/OCDB/newsilicates.html

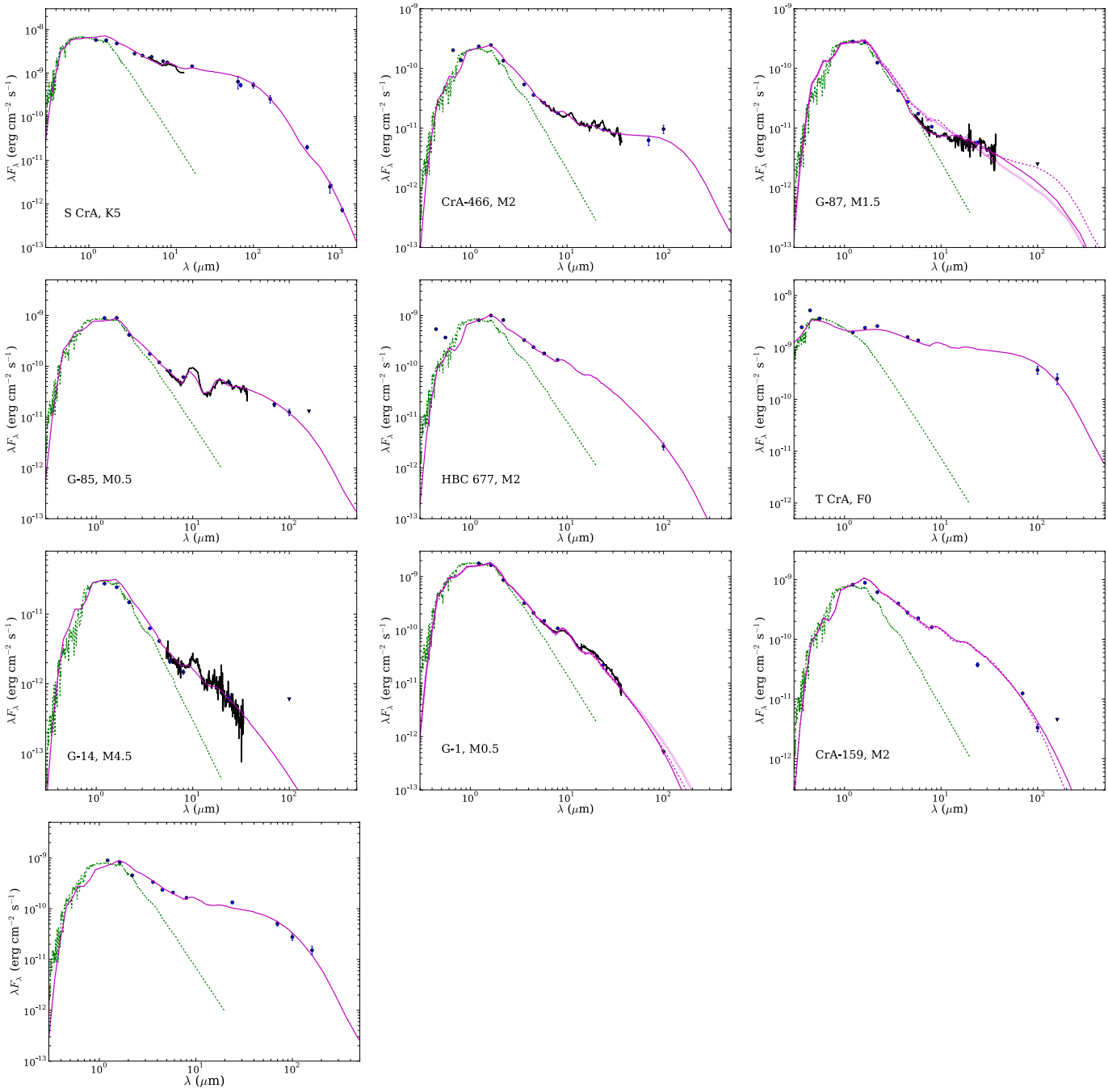

Fig. 12. SEDs and disk models. Photometry detections are marked as circles, with upper limits marked as inverted triangles. The spectra correspond to *Spitzer*/IRS observations, when available. For comparison, a photospheric MARCS model (Gustafsson et al. 2008) with a similar spectral type is shown for each object (green dotted line). The disk models are shown as magenta bold lines (or also dotted and dashed lines, in the cases with more than one model). See text and Table 6 for a detailed discussion.

also explain the low mass of the disk, but more observations are needed to test this hypothesis.

HBC 677 is very similar to CrA-159, although the lack of MIPS data results in a large unexplored region in its SED and thus a large unconstrained area in the disk parameter space. The larger vertical scale height and mass of this disk (compared to CrA-159) make it consistent with a CTTS disk, albeit with very low dust mass, compared to typical Taurus disks around similar stars (Andrews & Williams 2005).

The disk around G-1 was not detected by *Herschel*/PACS, but the object is located in a region free from extended emission, which allows us to place a very stringent upper limit to its 100 μm flux. This sets a strong constraint to the disk mass, which would be as low as $\sim 1 \times 10^{-6}\ M_{\odot}$. A simple model tends to overpredict the *Herschel* fluxes (dotted line for G-1 in Fig. 12). Disk truncation could be also invoked, as in CrA-159, to reduce the flux (dashed line), which could be a possibility since Köhler et al. (2008) suggested that this object could be a binary (0.22″ projected separation). In addition, a small-dust-only distribution in a very low mass disk provides a good fit (continuous line for G-1 in Fig. 12). The low near-IR excess points to a small vertical scale height, although given the very low mass of the disk, the object does not need to be dramatically settled and could be close to hydrostatic equilibrium. The *Herschel* data

Table 6. Disk models for the Coronet cluster members.

Object	$T_{\rm eff}$ (K)	R_* ($R_\odot$)	M_* ($M_\odot$)	$M_{\rm disk}$ ($M_\odot$)	$a_{\rm min} - a_{\rm max}$ (μm)	$H_{\rm rdisk}/R_{\rm disk}$	$T(R_{\rm in})$ (K)	$R_{\rm out}$ (AU)	Comments
S CrA	4500	3.60	1.5	3.8×10^{-2}	0.1–10000	0.30	1500	400	Massive, typical CTTS disk
T CrA	7000	1.14	4.0	3.8×10^{-3}	0.1–100	0.33	1500	300	Typical CTTS disk
CrA-466	3500	1.06	0.4	2.8×10^{-4}	0.1–100	0.1	1500	100	Typical CTTS disk
CrA-45	3700	1.62	0.6	1.5×10^{-4}	0.1–100	0.32	1500	100	Typical CTTS disk
CrA-159	3500	1.95	0.4	3.8×10^{-6}	0.1–100	0.33	1500	40	Thick, truncated or strongly depleted. Gap? (continuous line)
"	3500	1.95	0.4	5.4×10^{-6}	0.1–20	0.33	1500	100	Small grains only. Depleted. Gap? (dashed line)
HBC 677	3500	1.95	0.4	5.8×10^{-6}	0.1–100	0.32	1500	100	Low-mass disk, relatively thick
G-1	3900	2.50	0.6	$<1.2 \times 10^{-6}$	0.1–100	0.095	1500	100	Very dust depleted and settled (dotted line)
"	3900	2.50	0.6	$<3 \times 10^{-7}$	0.1–100	0.085	1500	30	Settled, truncated (dashed line)
"	3900	2.50	0.6	$<6 \times 10^{-7}$	0.1–20	0.095	1500	100	Small grains only, depleted (continuous line)
G-14	3500	0.41	0.3	$<9 \times 10^{-7}$	0.1–100	0.08	1500	100	Grain size differences between inner/outer disk
G-85[a]	3800	1.60	0.6	1.7×10^{-4}	0.1–2/0.1–100[a]	0.09/0.095[a]	1500/200[a]	100	Opt. thin inner disk/gap (pre-transitional)[a]
G-87	3700	1.15	0.5	$<1.6 \times 10^{-4}$	0.1–100	0.03	1500	100	Standard disk model (dashed line)
"	3700	1.15	0.5	$<1.6 \times 10^{-4}$	20–1000	0.02	1500	100	Large grains (dotted line)
"	3700	1.15	0.5	$<1.6 \times 10^{-4}$	20–1000	0.02	400	100	Best fit: Inner hole plus large grains (continuous line)

Notes. RADMC disk models for the Coronet cluster members. The stellar parameters ($T_{\rm eff}$, R_*) are determined from the optical observations and spectroscopy. The disk parameters are modified to reproduce the observed SED in the whole wavelength range, starting with the simplest possible model (see text). The disk masses are estimated assuming a gas-to-dust ratio of 100 and a collisional distribution for the dust with grain sizes $a_{\rm min} - a_{\rm max}$. In case of upper limits at PACS wavelengths, the corresponding disk masses are upper limits only. [(a)] Marks objects with a distinct inner and outer disks, so the given values correspond to the inner and outer disk. In case of different models, the comments include a reference to the appropriate figure.

thus confirm G-1 to be a good example of a globally dust depleted disk, as was previously suggested by the IR observations alone (Currie & Sicilia-Aguilar 2011). The IR observations of G-14 are also consistent with a globally dust depleted disk, although due to the lower luminosity of the object, the *Herschel* upper limits do not allow us to constrain the full dust content and vertical scale height.

The disk around G-85 is consistent with a pre-transitional disk with an inner gap (similar to those in Espaillat et al. 2010). The strong silicate feature and low near-IR excess requires the presence of small silicate grains in an optically thin environment, and the high flux at 100 μm reveals a relatively large total disk mass. While previous disk models classified this object as a typical CTTS disk (based on broad-band photometry), it is not possible to reproduce simultaneously the strong silicate emission and the large mid- and far-IR flux assuming a uniform disk with a single dust composition and a single density power law. The best results for a simple model are achieved if the disk is separated into an inner and an outer part at a distance of about 2 AU, with the inner part being flared and optically thin and the outer part being relatively massive and optically thick. The large silicate feature requires the inner disk to be populated by mostly small grains (here we assumed a flat distribution of grains with sizes 0.1−2 μm), while the outer disk is consistent with a standard dust grain distribution. Such filtered grain distributions have been predicted theoretically for disks with inner gaps and planets (Rice et al. 2006). An optically thick inner disk, followed by a relatively clean gap with small grains and an optically thick outer disk cannot be excluded either with the available observations.

Although undetected, the *Herschel* upper limit flux for G-87 puts strong constraints to its disk structure. Fitting of the G-87 disk, which has been successively regarded as a transition (Sicilia-Aguilar et al. 2008), primordial (Ercolano et al. 2009), and transition/homologously depleted (Currie & Sicilia-Aguilar 2011) disk, reveals that it is consistent with a low-mass disk ($M_{\rm d} < 3.2 \times 10^{-4}\ M_*$) with an inner hole. Assuming a standard dust distribution (0.1−100 μm, exponent −3.5) and varying the vertical scale height results in too high fluxes at $\lambda > 5$ μm for any values that reproduce the emission at 20−30 μm (see G-87 in Fig. 12, dashed line), which would have resulted at least in a marginal detection at 100 μm. The object has a small silicate feature and a large crystallinity fraction (Sicilia-Aguilar et al. 2008), which is typical of disks with strong grain growth where most of the amorphous grains are in aggregates a few microns in size. If we then change the dust distribution to reduce the amount of small dust (10−1000 or 20−1000 μm, exponent −3.5), the near-IR flux is reduced for sufficiently geometrically thin disks, but the emission in the 5−15 μm region is still too high (see G-87 in Fig. 12, dotted line). The best fit is achieved including an inner hole of about 0.3−1 AU in size, together with a grain population mostly consistent with large grains (10−1000 or 20−1000 μm, exponent −3.5; see G-87 in Fig. 12, continuous line). A small fraction of submicron and partly crystalline grains in the inner hole could account for the observed silicate feature. The models thus point toward the transitional nature of this object.

4.3. The disk-protostar connection?

To summarize the previous sections, despite the youth of the cluster, the Coronet region already shows a rich and diverse disk population, where the signs of disk evolution (depletion of small dust grains, inside-out evolution) are common. The masses of the disks are in general lower than what is typically observed

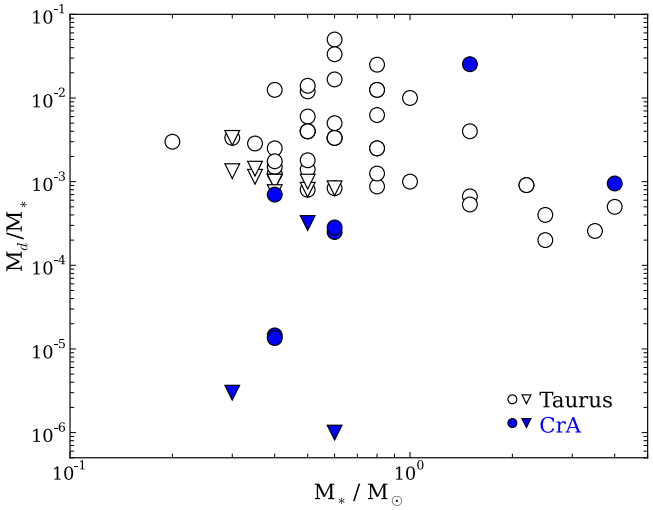

Fig. 13. Disk mass versus stellar mass in Taurus (Andrews & Williams 2005, open symbols) and in the CrA region (filled symbols). In both cases, inverted triangles mark upper limits. For objects with different disk models, we only display the mass derived from the best-fit model, although the differences in the masses between the models for each object are minimal thanks to the strong constraint provided by the PACS fluxes.

in clusters with similar ages. Figure 13 shows a comparison of the disk masses of the objects detected (or strongly constrained) wiht *Herschel* versus the stellar mass observed in Taurus (from Andrews & Williams 2005) with our results for the CrA region. Despite the small number of objects in the CrA region (10), we find that the disks around the M-type stars are significantly less massive than their Taurus counterparts. In particular, although there are a few Taurus disks with masses as low as those measured here, most of the Taurus disks are clearly more massive than the typical Coronet disks. Given the small size of the region in comparison with the typical sizes of star-forming *Herschel* filaments (Arzoumanian et al. 2011), it does not seem likely that the Coronet/CrA region is significantly older than Taurus. Although not all disks are detected with *Herschel*, the tendency would be toward detection of the most massive objects (at least, within a given spectral type range), which makes this difference even more striking. On the other hand, the more massive stars S CrA and T CrA have larger masses than the typical 1−2 $M_\odot$ star in Taurus. It is also remarkable that the objects with the largest disk masses or stronger PACS excesses among the solar-type and low-mass stars (S CrA, VV CrA, CrA-45) are not associated with the main cluster core, but rather lie on the outskirts of the dense cloud.

There are some differences in the way the Taurus disk masses are determined in Andrews & Williams (2005) and the masses derived for the CrA members by fitting their disks with RADMC. The main differences result from the dust opacity and the dust distributions considered. While the dust opacity in the millimeter is in both cases basically the same, changes in the β millimeter slope used by Andrews & Williams (2005) for deriving their dust masses can introduce a factor of a few difference between the derived masses. We therefore explored the resulting disk mass for the stars T CrA and CrA-466 by using different dust distributions with maximum grain sizes between 100 and 10 000 μm, finding variations up to a factor of ∼4 in the derived mass. This would result in a difference of 0.6 dex in Fig. 13, which would still place the CrA disks around low-mass stars among the less massive ones, compared to similar Taurus stars. A different mass analysis (Currie & Sicilia-Aguilar 2011), including only optical, 2MASS, and *Spitzer* observations, also confirms this trend toward lower masses compared to Taurus among the CrA members. A substantial amount of the dust mass could also be locked in larger grains, which cannot be excluded without more observations at longer wavelengths, although in this case it is unclear why grain growth would have proceeded more efficiently in the Coronet disks than in Taurus objects.

One potential explanation of this anomalous behavior of the disk properties could lie in the line of the arguments by Fang et al. (2013), who found a clear difference in the disk fraction vs. time in sparse cluster compared to more populous regions. While an exponential trend with a disk lifetime around 2−3 Myr is a very good approach for the disk fractions observed in more massive clusters (several hundreds of members) and OB associations (see also Fedele et al. 2010), a similar diagram for the sparse clusters (including the Coronet cluster) is harder to interpret. Very young regions have relatively moderate disk fractions that to a large extent survive over longer periods of time. Some authors have suggested that this behavior could be explained if the lifetimes of disks around binary stars were significantly shorter than the lifetimes of disks around single stars (Bouwman et al. 2006). In the case of the Coronet cluster, we do not have information about the multiplicity of most of the very low-mass stars, although most of the protostars are in multiple systems and a high degree of multiplicity has been suggested for many of the known TTS members (Köhler et al. 2008).

On the other hand, the *Herschel* data reveal that although the region is usually assumed to be relatively quiet due to the lack of very massive stars, the cluster center corresponds to a very crowded area, where the region around IRS 7 hosts about 20 objects (counting multiple systems, protostars, and the intermediate-mass stars R CrA and T CrA) within a region slightly less than 0.1 pc in diameter. Moreover, the *Herschel* data suggest strong interaction at least in some of the systems (IRS 5 complex), which are very likely to affect the formation of their disks. More observations of the region should be used to trace the early interactions of the systems and to quantify to which extent this may have contributed to shape the disks of the low-mass cluster members.

5. Summary and conclusions

We have presented *Herschel*/PACS observations at 100 and 160 μm of the CrA region. The observations covered the main parts of the Coronet cluster and detected many nearby YSOs, most of which are related to the central, denser part of the cluster with the strongest millimeter/submillimeter emission. Substantial cloud emission around the whole region was also revealed by the observations, including some details of spatially resolved sources. Most of the *Herschel* compact sources can be traced back to known submillimeter/millimeter condensations (consistent with protostellar objects or dense cloud parts) and to mid-IR sources identified as young T Tauri stars with disks.

1. Although *Herschel* reveals several extended structures following the path of the extinction maps, most of the star formation in the region, detectable as compact sources, is taking place in the central part of the cluster, which shows the higher densities and extinction (Kainulainen et al. 2009). Since *Herschel* is able to detect disks around very low-mass stars and very low-mass protostars, we can safely exclude active star formation in most of the cloud, which suggests a

poor efficiency or cloud densities below the threshold for star formation.

2. We are able to trace fine details of the structure of two Class I protostars, IRS 2 and the IRS 5 complex. The first is associated with a bubble-like structure, suggesting the expansion of a wide-angle wind in the molecular cloud material. The components of the IRS 5 multiple protostar, IRS 5a/b and the X-ray source FP-25, are surrounded by a filamentary extended structure that resembles the spiral arms that are usually associated to multiple systems by theoretical simulations of binary formation (Bate 2000). The size of the observed filaments is about seven times larger than the typical sizes predicted by the models, although the models are highly dependent on the initial angular momentum properties and on the mass of the protostars. Another possible explanation could be a swept-up, heated structure similar to what we find near IRS 2. Although IRS 5a/b are brighter in the near- and mid-IR and also at 100 μm, FP-25 is brighter at 160 μm, suggesting that it is in a more embedded, colder phase.
3. The components of the binary protostar IRS 7w/e are also resolved, although both are partially blended. IRS 7e, the faintest at wavelengths shorter than 100 μm, dominates at 160 μm. The region between IRS 7w and IRS 7e is clearly resolved at 100 μm, showing a decrease in emission. The Class 0 candidate source SMM 1 A is located to the south of both. Interestingly, the dip in far-IR emission between the three sources is coincident with the X-ray source FP-34 (Forbrich & Preibisch 2007), which could therefore be associated with a third embedded object or maybe with a jet/shock from any of the two protostars (there is other evidence of X-ray emission from optical jets in the region, see object G-80 in Sicilia-Aguilar et al. 2008).
4. The region presents objects in very early evolutionary stages. We confirm the sources SMM 1 A and SMM 1 As as Class 0 candidates with similar gray-body temperatures (16 K). On the other hand, the strong submillimeter emission to the north of the IRS 7 complex, named SMM 6 in Nutter et al. (2005) and also detected in our LABOCA maps (Sicilia-Aguilar et al. 2011a) appears as a dark lane in the 100 μm images and brigther at 160 μm, which is consistent with a starless core or maybe a pre-stellar condensation.
5. The *Herschel*/PACS data also reveal several very low-mass protostellar objects. The submillimeter source SMM 2 (Nutter et al. 2005) is probably an M-type Class I object. The mid-IR and X-ray source G-122 (Sicilia-Aguilar et al. 2008) is consistent with an even fainter very low-mass protostar. We also found a second condensation to the east of G-122, which is near the *Herschel*/PACS detection limit, but resembles G-122 in color and size.
6. The structure between the stars HD 176386 and TY CrA also revealed interesting characteristics. While the two objects display a double cavity in near- and mid-IR, the *Herschel*/PACS emission showed several peaks in the area in between the stars, which suggest that it could be related to heated, dense, compressed material (maybe a first step in triggered star formation). It is noticeable that the *Herschel* peak in this area does not coincide with the peak of 870 μm LABOCA emission, which is mostly centered (but extended) around HD 176386 and should mark the location of the densest cloud material. The whole region also shows strong radial striations, which could be a sign of large-scale collapse motions.
7. We also detected dust emission from the disks around several of the cluster members. To interpret the SEDs, we constructed radiative transfer models for the disks using the RADMC code (Dullemond & Dominik 2004). While the disk emission around the solar-type and intermediate-mass stars is consistent with flared, massive disks (S CrA, T CrA), the disks around the lower mass stars (spectral types M0 or later) have remarkably low masses ($M_{\rm d}/M_* < 10^{-3}$ $M_\odot$/yr). In some cases, the shape of the SED suggests either disk truncation (as for CrA-159) or strong dust depletion (as for HBC 677 and G-1). Some degree of inside-out evolution, such as inner holes or gaps, is also required to explain the full SEDs of some of the disks. In particular, G-85, which has a low near-IR flux, strong silicate feature, and relatively high far-IR flux , is best fitted including a gap at few AU, which would make it consistent with a pre-transitional disk. G-87 is best fitted by assuming a disk with strong grain growth and an inner hole, as we had previously inferred from its IRAC/IRS data (Sicilia-Aguilar et al. 2008).
8. While the masses of the disks around solar- and intermediate-mass stars are similar or higher than their Taurus counterparts, all M-type stars have disk masses that are systematically lower than the disk masses of other stars with similar ages (e.g. Taurus et al. 2005). This confirms our previous results inferred from the *Spitzer* observations (Sicilia-Aguilar et al. 2008; Currie & Sicilia-Aguilar 2011) that were initially interpreted as signs of evolution. The reduced mass of the disks could be either related to very marked early evolution, or be a result of the initial conditions in the star-forming cloud that could affect the structure of the disks. Given the youth of the cluster and that the present star-formation seems to be rich in multiple systems and shows signs of interactions between the stars and the parental cloud, the effect of initial conditions may have played an important role in shaping the disks. Observations in other clusters, that suggested differences in the disk fraction vs. time in sparse regions compared to more massive clusters (Fang et al. 2013), may also point in this direction.

Acknowledgements. This work is based on *Herschel*/PACS data. PACS has been developed by a consortium of institutes led by MPE (Germany) and including UVIE (Austria); KU Leuven, CSL, IMEC (Belgium); CEA, LAM (France); MPIA (Germany); INAF-IFSI/OAA/OAP/OAT, LENS, SISSA (Italy); IAC (Spain). This development has been supported by the funding agencies BMVIT (Austria), ESA-PRODEX (Belgium), CEA/CNES (France), DLR (Germany), ASI/INAF (Italy), and CICYT/MCYT (Spain). This work has made use of the SIMBAD database. It also makes use of data products from the Two Micron All Sky Survey, which is a joint project of the University of Massachusetts and the Infrared Processing and Analysis Center/California Institute of Technology, funded by the National Aeronautics and Space Administration and the National Science Foundation. We thank C. P. Dullemond for his help in providing the RADMC 2D code, and the anonymous referee for providing useful comments that helped to clarify this paper. A.S.A acknowledges support by the Spanish "Ramón y Cajal" program from the Spanish MICINN, grant number RYC2010-06164.

References

Acke, B., & van den Ancker, M. E. 2004, A&A, 426, 151
André, P., Men'shchikov, A., Bontemps, S., et al. 2010, A&A, 518, L102
Andrews, S., & Williams, J. 2005, ApJ, 631, 1134
Arzoumanian, D., André, P., Didelon, P., et al. 2011, A&A, 529, L6
Bate, M. R. 2000, MNRAS, 314, 33
Bast, J. E., Brown, J. M., Herczeg, G. J., van Dishoeck, E. F., & Pontoppidan, K. M. 2011, A&A, 527, A119
Beckwith, S. V. W., Henning, T., & Nakagawa, Y. 2000, in Protostars and Planets IV, eds. V. Mannings, A. P. Boss, & S. S. Russell (Tucson: University of Arizona Press), 533
Bibo, E. A., The, P. S., & Dawanas, D. N. 1992, A&A, 260, 293
Chen, H., Grenfell, T. G., Myers, P. C., & Hughes, J. D. 1997, ApJ, 478, 295

Chini, R., Kämpagen, K., Reipurth, B., et al. 2003, A&A, 409, 235
Currie, T., & Sicilia-Aguilar, A. 2011, ApJ, 732, 24
De Muizon, M., Rouan, D., Lena, P., Nicollier, C., & Wijnbergen, J. 1980, A&A, 83, 140
Dorschner, J, Begemann, B., Henning, T., Jäger, C., & Mutschke, H. 1995, A&A, 300, 503
Dullemond, C., & Dominik, C. 2004, A&A, 417, 159
Eiroa, C., Palacios, J., & Casali, M. 1997, ASPC, 119, 107
Espaillat, C., D'Alessio, P., Hernàndez, J., et al. 2010, ApJ, 717, 441
Fang, M., van Boekel, R., Bouwman, J., et al. 2013, A&A, 549, A15
Favata, F., Fridlund, C. V. M., Micela, G., Sciortino, S., & Kaas, A. A. 2002, ASPC, 277, 467
Forbrich, J., & Preibisch, T. 2007, A&A, 475, 959
Forbrich, J., Preibisch, T., & Menten, K. M. 2006, A&A, 446, 155
Garmire, G., & Garmire, A. 2003, Astron. Nachr., 324, 153
Garmire, G. P., Bautz, M. W., Ford, P. G., Nousek, J. A., & Ricker, G. R. 2003, Proc. SPIE, 4851, 28
Groppi, C. E., Kulesa, C., Walker, C., & Martin, C. L. 2004, ApJ, 612, 946
Groppi, C. E., Hunter, T. R., Blundell, R., & Sandell, G. 2007, ApJ, 670, 489
Gustafsson, B., Edvardsson, B., Eriksson, K., et al. 2008, A&A, 486, 951
Gutermuth, R. A., Megeath, S. T., Myers, P. C., et al. 2009, ApJS, 184, 18
Hamaguchi, K., Yamauchi, S., Koyama, K., et al. 2005, ApJ, 618, 360
Harju, J., Haikala, L. K., Mattila, K., et al. 1993, A&A, 278, 569
Hennemann, M., Motte, F., Schneider, N., et al. 2012, A&A, 543, L3
Henning, Th., Launhardt, R., Steinacker, J., & Thamm, E. 1994, A&A, 338, 223
Jäger, C., Mutschke, H., Begeman, B., Dorschner, J., & Henning, Th. 1994, A&A, 292, 641
Kainulainen, J., Beuther, H., Henning, T., & Plume, R. 2009, A&A, 508, L35
Kataza, H., Alfageme, C., Cassatella, A., et al. 2010, AKARI-IRC Point Source Catalogue Release note Version 1.0
Kley, W., & Burkert, A. 2000, in Disks, Planetesimals, and Planets, ASP Conf. Proc., 219, 189
Köhler, R., Neuhäuser, R., Krämer, S., et al. 2008, A&A, 488, 997
Kruger, A. J., Richter, M. J., Carr, J. S., et al. 2011, ApJ, 729, 145
Lindberg, J. E., & Jørgensen, J. K. 2012, A&A, 548, A24
López-Martí, B., Eislöffel, J., & Mundt, R. 2005, A&A, 444, 175
López Martí, B., Spezzi, L., Merín, B., et al. 2010, A&A, 515, A31
Loren, R. B. 1979, ApJ, 227, 832
Marraco, H. G., & Rydgren, A. E. 1981, AJ, 86, 62
Meyer, M. R., & Wilking, B. A. 2009, PASP, 121, 350
Myers, P. C., & Ladd, E. F. 1993, ApJ, 413, L47
Neuhäuser, R., Walter, F. M., Covino, E., et al. 2000, A&A, 146, 323
Nisini, B., Antoniucci, S., Giannini, T., & Lorenzetti, D. 2005, A&A, 429, 543
Nutter, D. J., Ward-Thompson, D., & André, P. 2005, MNRAS, 357, 975
Ott, S. 2010, in Astronomical Data Analysis Software and Systems XIX, ASP Conf. Proc., 434, 139
Peterson, D. E., Caratti o Garatti, A., Bourke, T. L., et al. 2011, ApJS, 194, 43
Pilbratt, G. L., Riedinger, J. R., Passvogel, T., et al. 2010, A&A, 518, L1
Poglitsch, A., Waelkens, C., Geis, N., et al. 2010, A&A, 518, L2
Ratzka, T., Leinert, C., Przygodda, F., & Wolf, S. 2008, The Power of Optical/IR Interferometry: Recent Scientific Results and 2nd Generation Instrumentation, ESO Astrophys. Symp. (Springer), 519
Rice, W., Armitage, P., Wood, K., & Lodato, G. 2006, MNRAS, 373, 1619
Roussel, H. 2012 [arXiv:1205.2576]
Sicilia-Aguilar, A., Henning, Th., Juhász, A., et al. 2008, ApJ, 687, 1145
Sicilia-Aguilar, A., Henning, Th., & Hartmann, L. 2010, ApJ, 710, 597
Sicilia-Aguilar, A., Henning, T., Kainulainen, J., & Roccatagliata, V. 2011a, ApJ, 736, 137
Sicilia-Aguilar, A., Henning, T., Dullemond, C. P., et al. 2011b, ApJ, 742, 39
Stutz, A. M., Rieke, G. H., Bieging, J. H., et al. 2009, ApJ, 707, 137
Taylor, K. N. R., & Storey, J. W. V. 1984, MNRAS, 209, 5
Tobin, J. J., Hartmann, L., Chiang, H.-F., et al. 2011, ApJ, 740, 45
Torres, C. A. O., Quast, G. R., da Silva, L., et al. 2006, A&A, 460, 695
Walter, F. 1986, ApJ, 306, 573
Walter, F., Vrba, F. J., Wolk, S. J., et al. 1997, AJ, 114, 1544
Wang, H., Mundt, R., Henning, Th., & Apai, D. 2004, ApJ, 617, 1191
Weidenschilling, S. J. 1977, Ap&SS, 51, 153
Wilking, B. A., Harvey, P. M., Joy, M., Hyland, A. R., & Jones, T. J. 1985, ApJ, 293, 165
Williams, J. P., de Geus, E. J., & Blitz, L. 1994, ApJ, 428, 693

Pages 21 to 26 are available in the electronic edition of the journal at http://www.aanda.org

Table 3. SED information for CrA members.

ID, RA Dec (J2000), A_V (mag)	λ (μm)	Flux (Jy)	Uncertainty (Jy)	References/Comments
CrA-432, 19:00:59.74 –36:47:10.9, A_V = 2.7[f]	0.66	7e-5	1e-5	LM05
	0.80	5e-4	1e-4	LM05
	1.22	3.3e-3	1e-4	2MASS
	1.63	4.7e-3	2e-4	2MASS
	2.19	4.7e-3	2e-4	2MASS
	3.6	4.5e-3	2e-4	SA08
	4.5	3.8e-3	3e-4	SA08
	5.8	3.5e-3	2e-4	SA08
	8.0	3.3e-3	3e-4	SA08
	23.9	3.1e-3	4e-4	SA08
	100	<0.019	–	TW
S CrA, 19:01:08.62 –36:57:20.3, A_V = 4.0[f]	1.22	0.828	0.019	2MASS
	1.63	1.54	0.04	2MASS
	2.19	2.29	0.05	2MASS
	3.6	2.66	0.01	CSA11
	4.5	3.16	0.01	CSA11
	5.8	3.81	0.02	CSA11
	8.0	4.17	0.02	CSA11
	9	4.41	0.08	AKARI
	18	7.19	0.10	AKARI
	65	13.8	4.3	IRAS
	70	12.4	1.2	TW
	100	17.7	2.6	TW
	160	13.6	2.7	TW
	450	3	0.3	N05
	850	0.7	0.2	N05
	870	0.77	0.02	SA11
	1200	0.29	0.03	Ch03
CrA-4110, 19:01:16.29 –36:56:28.2, A_V = 0.41[SA08]	0.66	4e-4	1e-4	LM05
	0.80	2.2e-3	1e-4	LM05
	1.22	0.0103	2e-4	2MASS
	1.63	0.0121	2e-4	2MASS
	2.19	0.0111	2e-4	2MASS
	3.6	9.1e-3	2e-4	SA08
	4.5	8.2e-3	2e-4	SA08
	5.8	5.7e-3	4e-4	SA08
	8.0	5.3e-3	2e-4	SA08
	23.9	7-9e-3	7e-4	SA08
	100	<0.025	–	TW
CrA-466, 19:01:18.93 -36:58:28.2, A_V = 8.1[SA08]	0.66	1e-46	1e-4	LM05
	0.80	1e-3	1e-4	LM05
	1.22	0.0115	3e-4	2MASS
	1.63	0.0324	9e-4	2MASS
	2.19	0.0419	1e-3	2MASS
	3.6	0.0402	4e-4	SA08
	4.5	0.0374	4e-4	SA08
	5.8	0.0356	1.1e-3	SA08
	8.0	0.0331	5e-4	SA08
	23.9	0.0522	1e-4	SA08
	70.0	0.146	0.027	TW
	100	0.32	0.05	TW

Notes. For each object, name and position (and extinction, where relevant) are listed, followed by the available observations and their references. The references are this work (TW); Wilking et al. (1997; W97); Bibo et al. (1992; B92); López-Martí et al. (2005; LM05); Cutri et al. (2003; 2MASS); Forbrich & Preibisch (2007; FP07); Acke & Van den Ancker (2004); Groppi et al. (2007; G07); Sicilia-Aguilar et al. (2008; SA08); Sicilia-Aguilar et al. (2011a; SA11); Currie & Sicilia-Aguilar (2011; CSA11); Peterson et al. (2011; P11); Kataza et al. (2010; AKARI); Chini et al. (2003; Ch03); Nutter et al. (2005; N05); IRAS database (IRAS); Bast et al. (2011; B11). The extinction of the sources comes either from the literature, or from our SED fitting (labeled with [f]). Potentially saturated photometry is marked by [s]. Fluxes with large uncertainties caused by nearby objects or cloud structures that make it difficult to delimit individual objects (IRS 7w/e, IRS 5a/b) are marked with [u].

Table 3. continued.

ID, RA Dec (J2000), A_V (mag)	λ (μm)	Flux (Jy)	Uncertainty (Jy)	References/Comments
G-87, 19:01:32.32 –36:58:03.0, A_V = 16[SA11]	1.22	1.80e-3	7e-5	2MASS
	1.63	9.1e-3	3e-4	2MASS
	2.19	0.0170	4e-4	2MASS
	3.6	0.020	1e-3	SA08
	4.5	0.020	1e-3	SA08
	5.8	0.0164	8e-4	SA08
	8.0	0.0137	7e-4	SA08
	23.9	0.022	2e-3	SA08
	100	<0.082	–	TW
G-85, 19:01:33.85 –36:57:44.8, A_V = 19[SA11]	1.22	2e-361	9e-5	2MASS
	1.63	0.0175	4e-4	2MASS
	2.19	0.0411	8e-4	2MASS
	3.6	0.0687	3e-4	SA08
	4.5	0.0760	3e-4	SA08
	5.8	0.0661	3e-4	SA08
	8.0	0.0691	3e-4	SA08
	23.9	0.162	2e-3	SA08
	70	0.41	0.04	TW
	100	0.42	0.06	TW
	160	<0.69	–	TW
G-122, 19:01:40.9 –36:57:15	3.6	2e-30	2e-4	SA08
	4.5	2.1e-3	2e-4	SA08
	5.8	6.8e-3	8e-4	SA08
	8.0	0.0147	4e-4	SA08
	23.9	0.123	6-3	SA08
	70	0.550	0.023	TW
	100	0.61	0.09	TW
	160	2.2	0.4	TW
IRS 2, 19:01:41.56 –36:58:31.2	1.22	5e-30	1e-4	2MASS
	1.63	0.129	4e-3	2MASS
	2.19	0.949	0.023	2MASS
	8.0	7.712:[s]	0.018	CSA11
	70	32.8	3.3	TW
	100	82	12	TW
	160	61	12	TW
	450	12	4	N05
	850	2.0	0.2	N05
	870	1.44	0.01	SA11
	1200	1.32	0.20	Ch03
HBC 677, 19:01:41.62 –36:59:52.7, A_V = 4.5[f]	0.44	3e-4	1e-4	SIMBAD
	0.55	1.1e-3	1e-4	SIMBAD
	1.22	0.102	3e-3	2MASS
	1.63	0.247	6e-3	2MASS
	2.19	0.37	0.01	2MASS
	3.6	0.302	2e-3	CSA11
	4.5	0.292	2e-3	CSA11
	5.8	0.279	2e-3	CSA11
	8.0	0.291	1e-3	CSA11
	100	0.089	0.014	TW
IRS 5a+b[u], 19:01:48.06 –36:57:22.0	1.63	3e-35	4e-4	2MASS
	2.19	0.060	3e-3	2MASS
	3.6	0.2925	4e-4	CSA11
	4.5	0.5464	6e-4	CSA11
	8.0	1.706	5e-3	CSA11
	70	17.3	1.7	TW
	100	19.4	2.8	TW
	160	23	5	TW, IRS 5ab+FP-25[u]

Table 3. continued.

ID, RA Dec (J2000), A_V (mag)	λ (μm)	Flux (Jy)	Uncertainty (Jy)	References/Comments
FP-25, 19:01:48.46 –36:57:14.9	2.19	6e-3	1e-3	2MASS
	3.6	8.1e-3	1e-4	CSA11
	4.5	0.0209	1e-4	CSA11
	5.8	0.0360	2e-4	CSA11
	8.0	0.0529	2e-4	CSA11
	100	15	3	TW
	160	23	5	TW, IRS 5ab+FP-25[u]
	450	12	4	N05
	850	1.8	0.2	N05
	1300	0.095	0.007	P11
IRS 6, 19:01:50.48 –36:56:38.4	1.22	4e-4	1e-4	2MASS
	1.63	<0.014	–	2MASS
	2.19	<0.048	–	2MASS
	3.6	0.1139	3e-4	CSA11
	4.5	0.1513	5e-4	CSA11
	8.0	0.1962	6e-4	CSA11
	23.9	0.348	0.035	P11
	70	5.30	0.5	TW
	100	9.2	1.3	TW
	160	11	2	TW
V 710, 19:01:50.68 –36:58:09.6	1.22	6.5e-4	6e-5	2MASS
	1.63	0.036	1e-3	2MASS
	2.19	0.570	0.026	2MASS
	4.5	6.178	0.018	CSA11
	70	108	11	TW
	100	97	14	TW
	160	70	14	TW
	450	9	3	N05
	850	1.5	0.2	N05
CrA-465, 19:01.53.74 –37:00:33.9, $A_V = 0.08^{SA08}$	0.66	7e-5	1e-5	LM05
	0.80	5e-4	1e-4	LM05
	1.22	3.7e-3	1e-4	2MASS
	1.63	4.5e.3	2e-4	2MASS
	2.19	4.0e-3	2e-4	2MASS
	3.6	3.4e-3	3e-4	SA08
	4.5	2.9e-3	2e-4	SA08
	8.0	2.5e-3	3e-4	SA08
	23.9	0.010	1e-3	SA08
	100	<0.027	–	TW
SMM 1A s, 19:01:54.9 –36:58:19	100	13	2	TW
	160	30	7	TW
	450	6.9	1.7	G07
	850	1.2	0.2	G07
IRS 7w, 19:01:55.32 –36:57:21.9	1.22	0.015	5e-3	2MASS
	1.63	5e-3	2e-3	2MASS
	2.19	0.031	0.01	2MASS
	3.6	0.0988	3e-4	CSA11
	4.5	0.2662	7e-4	CSA11
	70	234	36	TW
	100	476	69	TW[u]
	160	880	170	TW[u]
	450	45	15	N05
	850	5.6	0.6	N05
SMM 1 A, 19:01:55.5 –36:57:41	100	148	22	TW
	450	151	30	G07
	850	14.5	2.2	G07

Table 3. continued.

ID, RA Dec (J2000), A_V (mag)	λ (μm)	Flux (Jy)	Uncertainty (Jy)	References/Comments
SMM 2, 19:01:58.54 –36:57:08.5	1.22	2.3e-4	2e-5	2MASS
	1.63	6.3e-4	8e-5	2MASS
	2.19	2.01e-3	7e-5	2MASS
	3.6	0.0225	1e-33	P11
	4.5	0.0721	3e-38	P11
	5.8	0.136	8e-3	P11
	8.0	0.195	0.011	P11
	23.9	0.807	0.078	P11
	100	12	2	TW
	160	25	5	TW
	450	10	3	N05
	850	1.5	0.2	N05
	450	5.8	1.5	G07
	850	1.2	0.2	G07
	1300	0.135	0.027	P11
T CrA,19:01:58.78 –36:57:49.9, $A_V = 2.45^{AVA04}$	0.36	9e-3	5e-3	B92
	0.44	0.037	0.018	B92
	0.55	0.069	1e-3	B92
	1.22	0.421	0.014	2MASS
	1.63	0.846	0.033	2MASS
	2.19	1.460	0.035	2MASS
	4.5	2.124	9e-3	CSA11
	5.8	2.365	0.011	CSA11
	100	12	2	TW
	160	13	3	TW
B185839.6-3658, 19:02:01.94 –36:54:00.1, $A_V = 13^{FP07}$	1.63	1.6e-4	2.5	W97
	2.19	3.3e-4	2e-5	W97
	3.6	2.9e-4	3e-5	P11
	4.5	2.6e-4	2e-5	P11
	5.8	2e-4	1e-4	P11
	8.0	1.0e-3	1e-4	P11
	23.9	3.3e-3	4e-4	P11
	100	0.12	0.03	TW
G-14, 19:02:12.01 –37:03:09.3, $A_V = 1.9^{SA08}$	1.22	6.8e-3	2e-4	2MASS
	1.63	9.5e-3	3e-4	2MASS
	2.19	8.8e-3	2e-4	2MASS
	3.6	6.7e.3	3e-4	SA08
	4.5	5.7e-3	3e-4	SA08
	5.8	3.7e-3	3e-4	SA08
	8.0	3.6e-3	3e-4	SA08
	23.9	4.6e-3	5e-4	SA08
	100	<0.020	–	TW
CrA-4109, 19:02:16.67 –36:45:49.3, $A_V = 0^f$	0.66	1e-33	1e-4	LM05
	0.80	6.6e-3	1e-4	LM05
	1.22	0.0247	6e-4	2MASS
	1.63	0.0307	7e-4	2MASS
	2.19	0.0249	6e-4	2MASS
	3.6	0.0147	2e-4	SA08
	5.8	6.7e-3	6e-4	SA08
	23.9	0.0117	4e-4	SA08
	100	<0.018	–	TW
G-1, 19:02:27.08 –36:58:13.2, $A_V = 3.4^{SA08}$	1.22	0.297	8e-3	2MASS
	1.63	0.492	0.020	2MASS
	2.19	0.440	8e-3	2MASS
	3.6	0.311	2e-3	SA08
	4.5	0.269	1e-3	SA08
	5.8	0.245	2e-3	SA08
	8.0	0.246	1e-3	SA08
	23.9	0.151	1e-3	SA08
	100	<0.017	–	TW

Table 3. continued.

ID, RA Dec (J2000), A_V (mag)	λ (μm)	Flux (Jy)	Uncertainty (Jy)	References/Comments
CrA-159, 19:02:33.08 –36:58:21.2, A_V = 5.0[f]	1.22	0.0916	2.9e-3	2MASS
	1.63	0.201	5e-3	2MASS
	2.19	0.266	5e-3	2MASS
	3.6	0.356	0.019	P11
	4.5	0.335	0.020	P11
	5.8	0.347	0.017	P11
	8.0	0.339	0.017	P11
	23.9	0.238	0.022	P11
	70	0.29	0.03	TW
	100	0.111	0.016	TW
	160	<0.24	–	TW
CrA-4107, 19:02:54.64 –36:46:19.2, A_V = 0[f]	0.66	7e-4	1e-4	LM05
	0.80	3.9e-3	1e-4	LM05
	1.22	0.0166	4e-4	2MASS
	1.63	0.0195	5e-4	2MASS
	2.19	0.0174	4e-4	2MASS
	3.6	0.0143	1e-4	SA08
	5.8	0.0112	4e-4	SA08
	23.9	0.0114	4e-4	SA08
	100	<.018	–	TW
IRAS 18598, 19:02:58.56 –37:07:35.6, A_V = 5[f]	1.63	5e-4	1e-4	2MASS
	2.19	1e-3	1e-4	2MASS
	3.6	9.8e-3	4e-5	CSA11
	4.5	0.0224	4e-4	CSA11
	5.8	0.022	1e-3	CSA11
	8.0	0.0138	4e-4	CSA11
	23.9	2.474	1e-3	CSA11
	18	0.884	0.026	AKARI
	70	32.2	3.2	AKARI
	870	3.39	0.33	SA11
	1200	0.67	0.34	Ch03
	100	52	5	TW
	160	42	3	TW
	450	9	3	N05
	850	1.5	0.2	N05
	1300	0.103	0.008	P11
VV CrA, 19:03:06.80 –37:12:49.1, A_V = 15[f,B11]	1.22	0.179	5e-3	2MASS, SIMBAD
	1.63	0.729	0.030	2MASS, SIMBAD
	2.19	2.028	0.040	2MASS, SIMBAD
	3.6	4.753	0.017	CSA11
	4.5	6.160	0.022	CSA11
	5.8	15.21	0.05	CSA11
	9	24.1	0.2	AKARI
	18	39.7	4.3	AKARI
	12	31.9	3	IRAS
	25	69.1	7	IRAS
	60	131.0	13	IRAS
	100	95	10	IRAS
	70	55	6	TW
	100	80	12	TW
	160	66	13	TW
	450	12	4	N05
	850	2.0	0.2	N05
	870	1.66	0.06	SA11
	1200	0.58	0.06	Ch03

Table 3. continued.

ID, RA Dec (J2000), A_V (mag)	λ (μm)	Flux (Jy)	Uncertainty (Jy)	References/Comments
CrA-45, 19:03:16.09 –37:14:08.2, $A_V = 10^f$	1.22	0.0271	7e-4	2MASS
	1.63	0.0775	2e-3	2MASS
	2.19	0.1160	3e-3	2MASS
	3.6	0.223	0.012	P11
	4.5	0.224	0.012	P11
	5.8	0.256	0.013	P11
	8.0	0.278	0.014	P11
	23.9	0.676	0.063	P11
	70	1.18	0.12	TW
	100	0.92	0.13	TW
	160	0.81	0.16	TW